ALMA MATER STUDIORUM
UNIVERSITÀ DI BOLOGNA

ARCHIVIO ISTITUZIONALE
DELLA RICERCA

Alma Mater Studiorum Università di Bologna
Archivio istituzionale della ricerca

A multi-performance seismic design procedure to incorporate Crescent Shaped Braces in mid-rise frame structures

This is the final peer-reviewed author's accepted manuscript (postprint) of the following publication:

Published Version:
Michele Palermo, V.L. (2023). A multi-performance seismic design procedure to incorporate Crescent Shaped Braces in mid-rise frame structures. SOIL DYNAMICS AND EARTHQUAKE ENGINEERING, 164, 1-20 [10.1016/j.soildyn.2022.107625].

Availability:
This version is available at: https://hdl.handle.net/11585/905695 since: 2024-02-26

Published:

DOI: http://doi.org/10.1016/j.soildyn.2022.107625

Terms of use:

Some rights reserved. The terms and conditions for the reuse of this version of the manuscript are specified in the publishing policy. For all terms of use and more information see the publisher's website.

This item was downloaded from IRIS Università di Bologna (https://cris.unibo.it/).
When citing, please refer to the published version.

(Article begins on next page)

22 March 2025

A multi-performance seismic design procedure to incorporate Crescent Shaped Braces in mid-rise frame structures

Michele Palermo Ph.D[1], Vittoria Laghi Ph.D[1*], Giada Gasparini Ph.D[1], Stefano Silvestri Ph.D[1], Tomaso Trombetti Ph.D[1]

[*]*corresponding author: vittoria.laghi2@unibo.it*

[1]*DICAM – Department of Civil, Chemical, Environmental and Materials Engineering, University of Bologna, Italy*

Abstract

This paper introduces a novel procedure for the seismic design of a new class of seismic-resisting systems for mid-rise buildings obtained by incorporating special yielding steel braces known as Crescent Shaped Braces (CSBs) into not-moment-resisting frames. The proposed design procedure is grounded on the Performance-Based Seismic Design (PBSD) framework through the imposition of multiple seismic performance objectives with the aim of obtaining an almost uniform along-the-height seismic behavior. The desired uniform seismic behavior is ensured by imposing: (i) uniform inter-storey drifts under frequent earthquakes; (ii) widespread yielding of the braces along the building height under occasional earthquakes; (iii) minimum ductility capacity at all storeys to be exploited under rare earthquakes; (iv) minimum hardening stiffness for the mitigation of the second order (P-Δ) effects under very rare earthquakes. The desired performances are made possible by the specific features of the CSBs in terms of initial lateral stiffness, yielding strength, ductility capacity and final hardening response. The procedure is articulated in four conceptual phases and several steps to guide the professional engineer through all the main design phases, from the selection of the seismic performance objectives to the preliminary sizing of the CSB devices, up to the final design/verification through non-linear time history analyses. The effectiveness of the proposed design procedure is finally demonstrated through an applicative example.

Key words

Performance-Based Seismic Design; Crescent Shaped Braces; multiple performance objectives; uniform inter-storey drifts; minimum ductility capacity, P-Δ effects

1. Introduction

The conceptual framework of Performance Based Seismic Design (PBSD) first proposed by SEAOC [1] aims at evaluating the seismic response of a building towards predictable and controlled seismic performance parameters under established multiple earthquake intensity levels [2]. The PBSD principles foster the transition from a "passive" to an "active" structural design encompassing the following main phases (i) selection and identification of the desired performance objectives, (ii) conceptual design (e.g. identification of the most suitable structural solution) and first sizing of the structural elements (iii) final design with all necessary calculations, verifications and detailing to fulfill the code prescriptions.

In the last decades, different strategies and solutions have been proposed to fulfill PBSD principles through enhanced seismic performances with respect to those offered by conventional Moment-Resisting Frames (MRFs) and Concentrically-Braced Frames (CBFs), including base isolation [3], passive and active dissipative systems [4], coupled/dual systems [5], rocking walls [6], strongback systems [7–9], enhanced bracing systems [10–12]. Among different yielding braces, Buckling-Restrained Braces (BRBs) provide a symmetric response in tension and compression, through the improved performances against buckling, and have also been recently proposed as retrofitting solutions [13,14]. More recently, a post-tensioned self-centering yielding brace has been investigated by Nobahar et al. [15]. Other examples include pipe-based dampers [16], J-dampers [17,18], X-plate dampers [19] and steel shear panel-based dampers [20,21]. Alternative shapes for metal dampers have also been investigated over the past years. Hsu et al. studied the performances of steel-curved dampers used as bracing systems [22,23]. Jia et al. developed a novel fish-bone shaped buckling-restrained brace with improved performances [24]. Alternative solutions also see the application of hysteretic dampers in beam-column steel connections (see e.g. [25]). More recently, Guo et al. [26] proposed a new S-shaped mild steel damper. Xu and Ou studied a combined rotational friction and flexural yielding metallic damper (FD-MD) capable of providing an alternative for precast structures in high seismic regions [27]. In most cases, seismic design is developed only with reference to a single performance objective (PO) (e.g. a single performance point within the so-called Capacity Spectrum method [28]), and then final verifications are carried out with reference to the other POs established by the PBSD.

In this respect, a novel curved yielding brace, called Crescent Shaped Brace (CSB), has been proposed and investigated by the authors since 2009 [29–32] for a seismic design developed to meet multiple POs. Indeed, the curved shape of the CSB allows to customize the force-displacement hysteretic curve

with the possibility of covering various ranges of stiffness, strength, ductility and dissipative capacities, and thus to meet multiple performance points. In previous studies the mechanical behavior of the single CSB device has been first investigated through analytical methods to assess the elastic behavior up to the first yielding point. Then, the full non-linear inelastic behavior (both in tension and compression) has been evaluated through numerical and experimental studies up to failure [30,33]. In addition, some design procedures have been proposed for two specific applications: (i) insertion of CSBs at the first-storey only [30] to exploit the concept of soft-storey isolation first proposed by Fintel and Khan in 1968 [34], (ii) insertion of CSBs as diagonal braces in low-rise frame structures with direct computation of the global stiffness matrix [32]. The latter procedure is not applicable to more complex structures for which the direct computation of the global stiffness matrix becomes cumbersome.

More recently, direct analytical equations were obtained for preliminary design purposes to correlate the target mechanical parameters required by the PBSD framework (seismic base shear, ductility capacity, hardening, energy dissipation, …) with the geometrical and mechanical parameters of the CSBs [35]. A design approach is here proposed which encompasses the following design phases (Figure 1): (A) identification of the seismic performance objectives for the whole structure (target performances) taking into account the intended use of the structure, its strategic importance, any economic issues, etc.; (B) evaluation of the target mechanical parameters of each component of the lateral-resisting system; (C) evaluation of the actual geometrical and material properties of each component of the lateral-resisting system (i.e. sizing of the CSB); (D) final verification of the actual seismic performances of the whole structure (capacity curve through pushover analysis and performance points through non-linear time history analyses).

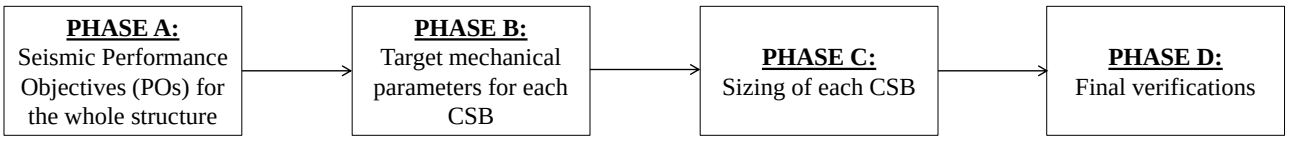

Figure 1: Schematic representation of the phases of the proposed design approach.

A similar approach has been applied to design a two-storey one-bay prototype frame braced with CSBs [36,37]. In that case, three POs have been identified for the prototype frame tested under reversed quasi-static cyclic lateral loads. The experimental results proved that the CSBs may represent a feasible solution for high-performances braced frame structures, able to satisfy multiple target seismic performance objectives (technology validation in a laboratory environment, corresponding to a TRL=4).

This work proposes an innovative step-wise design procedure, grounded on the design approach represented in Figure 1, for the insertion of CSBs as enhanced diagonal braces in mid-rise Not Moment-Resisting pinned Frame (NMRF) buildings. The novel structural system will be hereafter synthetically referred to as CSB Frame (CSBF). Since NMRFs do not contribute to carry lateral loads, the CSBs are the only components of the lateral-resisting system and therefore can be designed to exploit their full potential in terms of the desired non-linear force-displacement behavior. The innovative aspect of the proposed design procedure is twofold. On one hand, the coupling of a mid-rise multi-storey NMRF devoted to withstand vertical loads only with CSBs having the function of lateral-resisting system. On the other hand, the desired seismic performances for the whole structure leading to an "almost" uniform seismic behavior in terms of: (i) uniform along-the-height inter-storey drift (ID) profile, (ii) controlled yielding of all the CSBs along the height, (iii) minimum ductility capacity at all storeys, and (iv) minimum post-yielding hardening stiffness to mitigate second order (P-Δ) effects and reduce residual displacements. In this work, the latter aspect related to the mitigation of P-Δ effects is addressed in two ways: (1) with the introduction of a number of additional modification factors λ to be used in the preliminary design phase, and (2) through the development of a numerical case study dealing with the comparison of the seismic response with and without consideration of second-order effects.

The paper is organized as follows. Section 2 illustrates the main features of CSBs highlighting the expected superior performances of CSBFs with respect to conventional CBFs. Section 3 introduces the proposed seismic design procedure, that is then applied in Section 4 to a 10-storey one-bay CSB frame as illustrative example. In the applicative example the performances of the CSBF are compared with those of a CBF equipped with concentric diagonal braces (CBs) designed to obtain the same initial stiffness of the CSBF.

2. The expected seismic performances of CSBF structures

2.1. The main features of CSBs: geometrical, mechanical properties and design equations

In this section the main features of CSBs are briefly recalled. The CSB device is graphically represented in Figure 2a. The device is schematized as two straight elements of equal lengths L^* (symmetrical bilinear CSB) and initial inclination θ_0 from the horizontal direction. The extremes are hinged so no rotational restraint is provided. One of the extremes (point B) is free to move along the horizontal direction u. One of the main geometrical parameters governing the CSB behavior is the

initial lever arm d_0 (suffix "0" stands for the initial configuration), also written in normalized form $\xi_0=d_0/2L_0$. The value of d_0 has proved to severely influence the mechanical response of the CSB. Indeed, force-displacement responses both in tension and compression (Figures 2b and c) are governed by the interaction between the mechanical non-linearity of the material and the geometrical non-linearity resulting from the variation of the initial lever arm d_0 which strongly affects the axial-flexural interaction. This aspect has been recently investigated with analytical models that clarified the role of the lever arm on the transition between the flexure-controlled and the axial-controlled portions of the tensile force-displacement response of the CSB (Figure 2b) described by key performance points [35]. In particular, the force-displacement response in tension is qualitatively shown in Figure 2b evidencing the main behaviour regions with different colors. The first elastic region is characterized by an initial linear elastic behavior (with initial lateral stiffness k_{IN}) up to the flexural yielding point P_{fy}, followed by a pseudo-plastic plateau (plastic flexural region) governed by flexure up to the geometric hardening region, starting at point P_{gh} and ending at point P_{ay}, followed by the final plastic axial region. The extent of the pseudo-plastic plateau region limited by the two points P_{fy} and P_{gh} governs the ductility μ of the CSB. For illustrative purposes, the influence of ξ_0 on the shape of the *F-u* curve is qualitatively represented in Figure 2d. The in-plane force-displacement response in compression (qualitatively shown in Figure 2c) is characterized by a first elastic phase, concluded by the achievement of the yielding moment of the knee-point cross-section (point P_c in Figure 2c), followed by a softening branch governed by geometrical non-linearity. The key performance points of the force displacement response in tension (P_{fy}, P_{gh} and P_{ay}) and compression (P_c) are identified in Figures 2b and c. Further details are provided in [35].

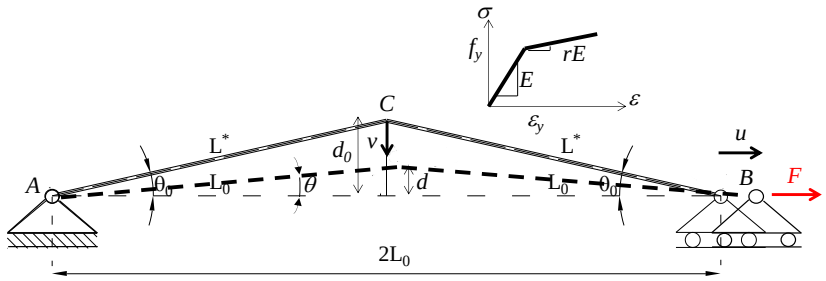

(a)

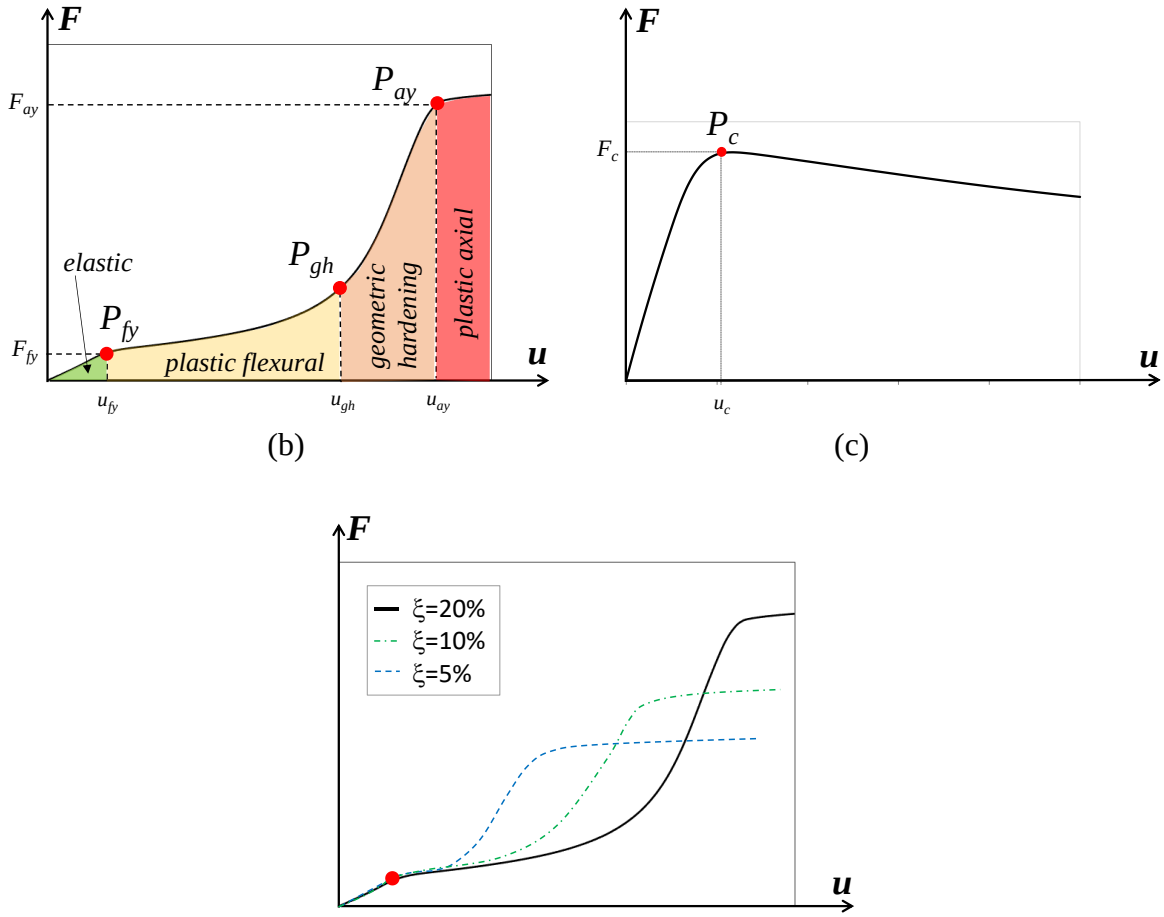

Figure 2: (a) The "symmetric bilinear" configuration of a CSB subjected to a lateral force *F*. (b) Force-displacement response in tension. (c) Force-displacement response in compression (not in scale with respect to the curve in tension). (d) The influence of ξ_0 on the force-displacement response in tension. Adapted from [35].

In order to guide the identification of the optimal CSB device, design equations (provided in the Appendix) are drawn to correlate the target mechanical parameters of the CSB (for instance the target initial stiffness $\overline{k_{IN}}$, the target yielding strength $\overline{F_y}$ and the target ductility capacity $\overline{\mu}$) with its main geometrical parameters ξ_0, *h* and *J*.

2.2. Comparing the seismic performances of CBFs and CSBFs

This section compares, from a conceptual point of view, the behavior of a CBF and a CSBF. For illustrative purposes, without loss of generality, a 10-storey one-bay structure is considered. The

columns are pinned at the base, as well as between consecutive storeys, thus leading to a NMRF structure. Also, the beams and the braces are connected to the columns by means of pinned connections. As mentioned before, since a NMRF is not able to withstand any lateral load, the resistance against horizontal actions has to be provided entirely by the braces. Figure 3 compares the behavior of the same NMRF equipped with CBs and with CSBs. The CBF (Figure 3a) behaves as a truss system with both columns and CBs subjected to axial forces only, which increase going from top to bottom storeys. In the CSBF (Figure 3b), the columns are subjected to axial forces only, while the CSBs are subjected to combined axial forces and bending moments due to the presence of the initial lever arm d_0. Therefore, while in a CBF both the lateral stiffness and strength depend uniquely on the axial behavior of the braces, in a CSBF the coupled flexural-axial response of the CSBs enables additional freedom in fine tuning the lateral response, as it will be shown in the next sections.

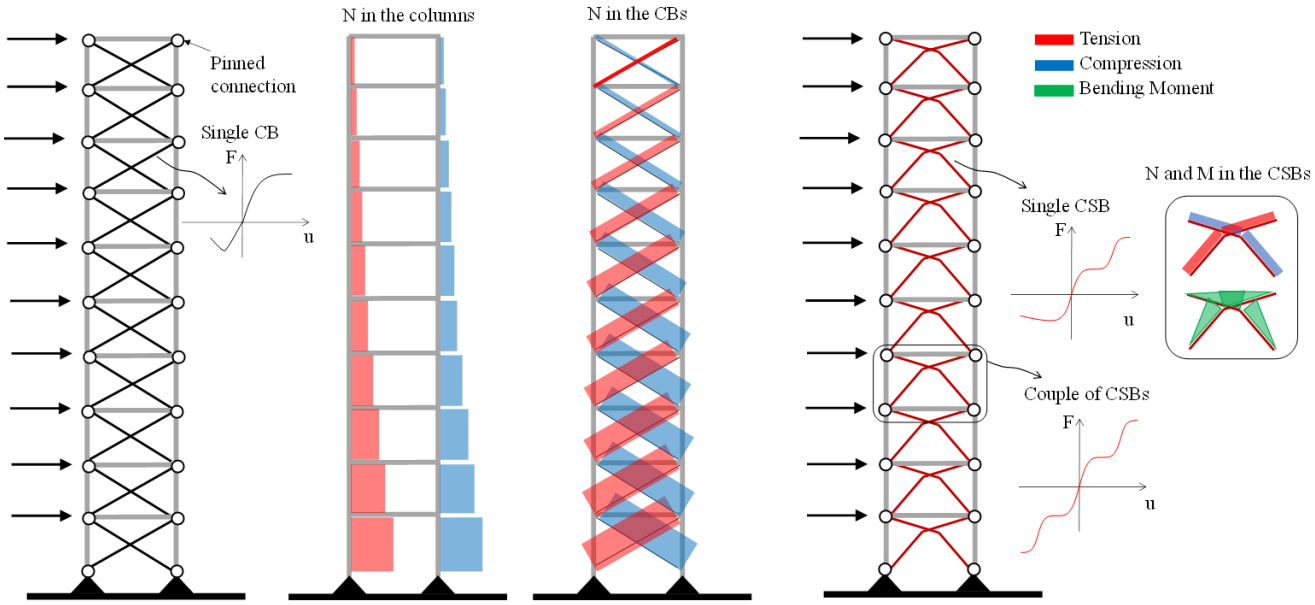

Figure 3: (a) Behavior of a CBF subjected to lateral loads; (b) behavior of a CSBF subjected to lateral loads.

2.3. Desired seismic performances of Uniform CSBFs

The proposed design procedure, that will be illustrated in detail in Section 3, guides the designer to obtain, through the imposition of specific seismic performance objectives (phase A), a structural system with the following desired seismic performances:

- uniform ID profile along the height of the structure under a frequent earthquake design level (first performance objective PO1, see Section 3.3);

- along the height yielding of the braces under an occasional earthquake design level (second performance objective PO2, see Section 3.4);

- minimum ductility capacity at all storeys to ensure diffuse plasticization, avoid large discrepancies in the peak inter-storey drifts and reduce the risk of dangerous localized damages possibly leading to soft/weak storey mechanisms under a rare earthquake design level (third performance objective PO3, see Section 3.5);

- minimum final hardening stiffness to mitigate second order (P-Δ) effects and residual drifts and reduce the risk of global instability/collapse under a very-rare earthquake design level (fourth performance objective PO4, see Section 3.6).

A frame system braced with CSBs undergoing these performances will be hereafter synthetically referred to as "Uniform CSBF".

Figure 4a qualitatively illustrates the target capacity curves of different CSBs in terms of the resistance provided by the CSB along the diagonal direction (F) vs the lateral inter-storey drift (δ) ignoring the second order effects associated to the presence of axial forces in the columns (e.g. P-Δ effects). Similarly, Figure 4b qualitatively illustrates the target capacity curve of a Uniform CSBF in terms of global base shear (V_{base}) vs lateral displacement of a specific control point (for instance, the roof displacement d_{roof}) ignoring the second order effects associated to the presence of axial forces in the columns (e.g. P-Δ effects). The four Performance Points (PPs) corresponding to the four seismic performance objectives (POs) identified in the first phase of the design approach (Phase A) are indicated with colored dots. The global target capacity curve of the whole lateral-resisting system (phase D) results from the contribution of each CSB device (phase C). The contribution of the single CSB to the global target capacity curve is discussed in detail in section 3.2, also highlighting the consequences related to the P-Δ effects.

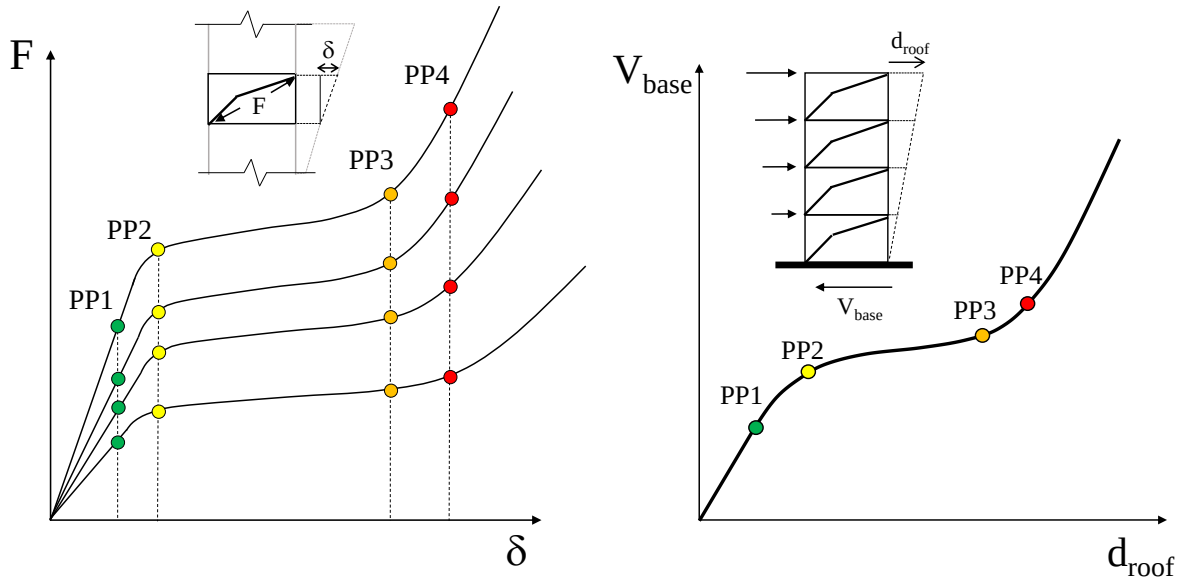

(a) (b)

Figure 4: (a) Qualitative representation of the force vs inter-storey drift target capacity curves of the single CSB located at different storeys ignoring P-Δ effects; (b) Qualitative representation of the base shear vs roof displacement target capacity curve of the Uniform CSBF ignoring P-Δ effects.

3. Seismic design procedure for Uniform CSBFs

3.1. Overview of the design procedure

Figure 5 provides the general flowchart of the proposed step-wise seismic design/verification procedure. In detail, the procedure is based on the four conceptual phases presented in Figure 1 (from A to D) articulated in 7 operational steps. It is mainly targeted to professional engineers with the purpose of reducing the computational effort typical of more complex design procedures requiring the implementation of sophisticate optimization algorithms requiring ad-hoc tools and software, typically beyond the expertise of common practitioners.

The starting phase (phase A) consists in the identification of the seismic performance objectives (POs) for the whole CSBF (STEP 1), which are the set of desired structural performances (target performances) under the selected multiple earthquake design levels (EQs). Reference is here made to the four performance objectives established by [38].

In phase B, four relevant performance points (PPs) of the target capacity curves of each individual CSB are determined by imposing the four POs. These performance points allow then to identify the target mechanical parameters of each CSB (STEPS 2-5).

In phase C, the CSBs are sized in terms of their geometrical and material properties, based on the target mechanical parameters obtained in the previous phase, using the design equations reported in Appendix or, alternatively, performing numerical simulations (STEP 6). To help the designers in the identification of the most suitable geometry and cross-section profiles for the CSBs, also design charts (such as those represented in Figure 2d) can be used. Clearly, the real capacity curves of the CSBs will slightly differ from the target ones. Hence, in phase D, non-linear time-history analyses and verifications will be performed. More in detail, the final step (STEP 6) consists in both global verification of the actual capacity curve through non-linear static analysis and local verifications of all structural elements through non-linear time-history dynamic simulations.

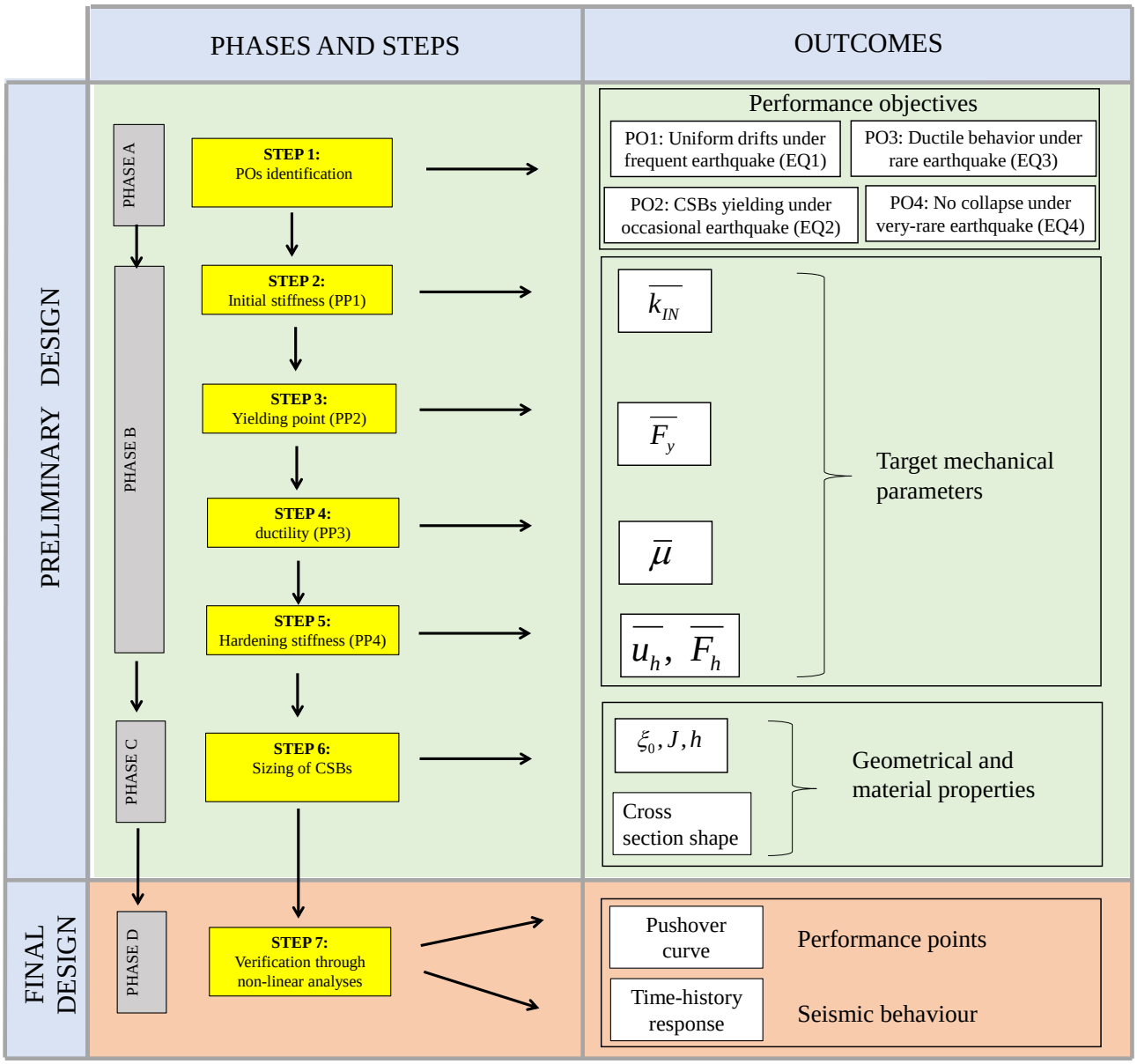

Figure 5: Overview of the proposed step-wise design procedure.

3.2. STEP 1: Identification of the seismic Performance Objectives and target capacity curves with and without consideration of P-Δ effects

Four POs are identified for the Uniform CSBF:

- PO1: No damage under Frequent earthquake. The building has to remain fully operational (i.e., in the elastic field) under the frequent design level EQ1. It is achieved by determining the target initial stiffness $\overline{k_{IN}}$ of each CSB in order to have uniform inter-storey drifts along the building height.
- PO2: First yielding under Occasional earthquake. The building has to remain in operational conditions (limited and repairable damage) under occasional design earthquake level EQ2. It is achieved by determining the target yielding strength $\overline{F_y}$ of each CSB in order to ensure an almost simultaneous yielding of all the CSBs.
- PO3: Life safety under Rare earthquake. The safety of the occupants has to be guaranteed under the rare earthquake design level EQ3. It is achieved by determining the minimum target ductility $\overline{\mu}$ of each CSB in order to guarantee a diffuse plasticization of all the CSBs.
- PO4: Collapse prevention under Very Rare earthquake. The global instability/collapse of the building has to be prevented under the very rare earthquake design level EQ4. It is achieved by determining the minimum hardening stiffness and ultimate capacity of the CSBs to ensure the global stability of the whole structure.

For each selected PO, Table 1 provides the considered earthquake design level (typically expressed in terms of a ground motion having a certain probability p of being exceeded within a given time frame V_R, e.g. having a certain return period T_R). For each earthquake design level, the required structural performance level, the corresponding engineering demand parameter, the performance point and the corresponding target mechanical parameter to be determined for each CSB device are also reported.

Table 1: Seismic performance objectives for the Uniform CSBF.

	Earthquake design level	**Structural performance level**	**Engineering Demand Parameter**	**Performance Point on the F-δ curve of each CSB**	**Target CSB mechanical parameters**
PO1	EQ1 (p=80% within V_R)	No damage	Inter-storey drift (ID) ratio	$PP1$	$\overline{k_{IN}}$
PO2	EQ2 (p=50% within V_R)	First yielding	First yielding strength	$PP2$	$\overline{F_y}$

PO3	EQ3 (p=10% within V_R)	Life safety	Ductility demand	*PP*3	$\overline{\mu}$
PO4	EQ4 (p=5% within V_R)	Collapse prevention	Final hardening providing over-strength and ultimate displacement capacity	*PP*4	$\overline{u_h}$, $\overline{\Delta F_h}$

The structural performances are typically quantified in terms of one or more Engineering Demand Parameters [38], that, in general, could be defined both at the whole structure level and at the single structural element level. In this specific case, the target structural performance associated to PO1 consists in limiting all peak ID ratios to the same target value ($\overline{ID}$). It is achieved by ensuring a target initial stiffness $\overline{k_{IN}}$ for each CSB. The target structural performance associated to PO2 is a minimum yielding strength for the whole lateral-resisting system (base shear capacity) that is achieved by ensuring a target yielding strength for each CSB ($\overline{F_y}$). The target structural performance associated to PO3 is the uniform plasticization of the CSBs along the height that is achieved by ensuring a proper ductility capacity ($\overline{\mu}$) for each CSB, evaluated from the ductility demand resulting from the seismic design intensities at EQ2 and EQ3. The target structural performance associated to PO4 consists in a minimum capacity to be ensured by the final hardening branch of the CSB (providing an over-strength capacity equal to $\overline{\Delta F_h}$, leading to a total strength capacity $\overline{F_h}$ at displacement $\overline{u_h}$).

Figure 6 provides a qualitative representation of the idealized target capacity curve in terms of force along the diagonal direction vs elongation along the diagonal direction (*F*-*u*) of the generic CSB when inserted in a frame. The angle ϑ indicates the inclination of the diagonal projection of the CSB with respect to the horizontal direction. Two families of curves are depicted. The black curves are obtained ignoring the P-Δ effects. The grey curves account for the P- Δ effects. In general, all target capacity curves are composed by: (1) a first linear elastic branch (where the performance point *PP*1 is located) with slope equal to $\overline{k_{IN}}$ up to the performance point *PP*2, characterized by yielding strength $\overline{F_y}$ and yielding displacement $\overline{u_y}$; (2) a pseudo-plastic branch characterized by the target minimum ductility $\overline{\mu}$ allowing to identify the performance point *PP*3; (3) a hardening branch containing the performance point *PP4* which is identified by imposing a minimum capacity in terms of strength $\overline{F_h}$ and displacement $\overline{u_h}$.

It should be first noted that the target yielding strength $\overline{F_y}$ is here assumed as the force leading to the formation of the plastic hinge at the knee cross-section of the CSB, thus accounting for the benefit corresponding to the cross-sectional shape factor β. It could be also noted that several trilinear relationships may be identified to satisfy the same target objectives. Clearly, the actual capacity curves of CSBs will be characterized by a smoother behaviour, as qualitatively shown in Figure 4.

The P-Δ effects can be visualized as a negative geometric stiffness of slope equal to k_G = - P/H which reduces the actual stiffness of the target capacity curve obtained ignoring the P-Δ effects ([39]). Clearly, the relative importance of the P-Δ effects depends on two main factors: the demand in terms of lateral displacement related to the earthquake intensity level and the amplitude of the vertical loads P, mainly related to the building height. Typically, for low earthquake intensity levels and low-to-mid-rise buildings, it is expected that the structure responds essentially in the elastic field with an initial stiffness significantly higher that the negative stiffness (given the limited amplitude of the vertical loads). Consequently, in these cases, the P-Δ effects have a minor impact on the seismic response of the structure and can be neglected in the preliminary design. Instead, for higher earthquake intensity levels and mid-to-high rise buildings, a seismic response within the inelastic field is typically permitted with higher displacement demand and reduced effective lateral stiffness. Therefore, in these cases, the P-Δ effects may have a significant impact on the seismic behavior of the structure, increasing the seismic displacement demand and reducing the reserve strength.

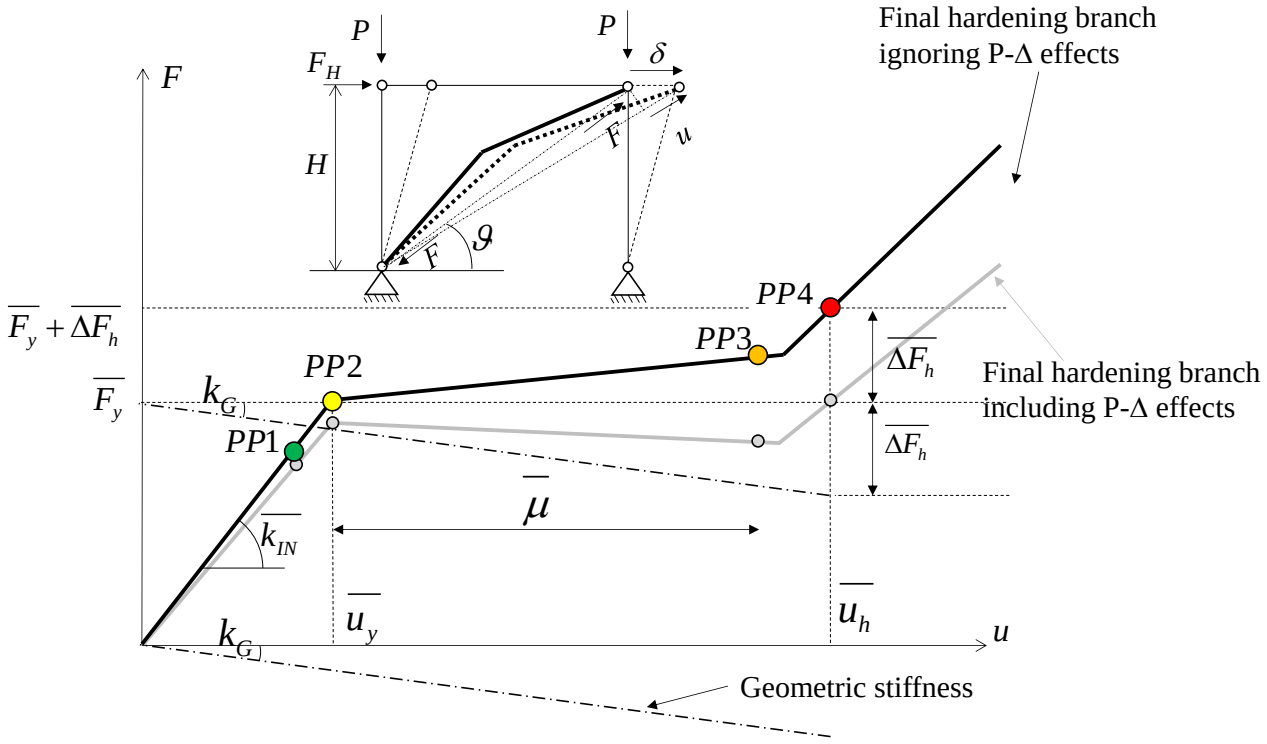

Figure 6: Possible target capacity curves for a single CSB satisfying the four POs, with and without consideration of P-Δ effects.

The next sections provide the practical indications to develop the preliminary design aimed at the first sizing of the CSBs to fulfill the target POs. The first and second POs are imposed by performing linear dynamic time-history analyses with the CSBs modelled as equivalent linear elastic springs. Therefore, the target initial stiffness and yielding strength of the CSBs are first determined without explicit consideration of the P-Δ effects, which can be then considered (if relevant) by applying specific modification factors (referred to as λ_1 and λ_2) whose values can be calibrated by means of specific non-linear dynamic time-history analyses. However, the calibration of the specific values of the modification factors is out of the scope of the present work.

The proposed procedure based on linear dynamic time-history analyses is suggested for relatively stiff mid-rise structures whose dynamic behavior under low intensity earthquake is not significantly affected by second order effects. Alternatively, when dealing with more flexible structures that are potentially prone to significant second order effects, the linear dynamic time history analyses could be replaced by non-linear dynamic time history analyses considering geometrical second order effects.

The third PO is determined analytically by comparing the elastic design spectra corresponding to EQ2 and EQ3. The fourth PO is determined analytically by explicit consideration, in a simplified way, of the P-Δ effects.

3.3. STEP 2: Initial stiffness and point PP1

The target structural performance associated to PO1 is the limitation of all peak ID ratios to the same target value $\overline{ID}$ under the frequent earthquake design level EQ1. It is achieved by calibrating the initial elastic lateral stiffness of each CSB ($\overline{k_{IN}}$) by means of an iterative procedure (inspired by the work by Lavan and Levy [40]) in order to satisfy the limitations in terms of peak ID ratios as prescribed by current seismic codes.

For this aim, a linear Finite Element (FE) model should be developed with each CSB modelled as an equivalent elastic spring characterized by initial (superscript 0 stands for the initial phase before the iterations) stiffness value $k_{el,i}^{\ 0}$ (with *i* indicating the generic *i*-th CSB). In order to determine the final target initial stiffness of each CSB, an iterative procedure is performed. At the beginning of the procedure, linear dynamic time-history analyses (considering an ensemble of ground motions consistent with the design earthquake level EQ1) are performed considering the linear FE model with

the initial elastic springs $k_{el,i}{}^{0}$. From the outcomes of the analysis, the average (over the accelerograms of the ensemble) peak ID ratio profile ($ID_{EQ1,j}{}^{0}$ with *j* indicating the *j*-th storey) is determined and compared with the target value $\overline{ID}$ in order to compute the discrepancies $\Delta ID_j{}^{1} = ID_{EQ1,j}{}^{0} - \overline{ID}$. Then, at the first iteration (identified by superscript 1), the stiffness of the *i*-th spring located at the *j*-th storey is updated to $k_{el,i}{}^{1} = k_{el,i}{}^{0} + \Delta k_{el,i}{}^{1}$ with $\Delta k_{el,i}{}^{1}$ proportional to $\Delta ID_j{}^{1}$:

$$\Delta k_{el,i}{}^{1} = k_{el,i}{}^{0} \cdot \frac{\Delta ID_j{}^{1}}{\overline{ID}} \tag{1}$$

The stiffness of the springs is then updated accordingly and the average peak ID ratio profile is recomputed.

Similarly, at the generic *k*-th iteration the stiffness of the *i*-th spring located at the *j*-th storey is modified by a quantity $\Delta k_{el,i}{}^{k}$ proportional to $\Delta ID_j{}^{k} = ID_{EQ1,j}{}^{k-1} - \overline{ID}$:

$$\Delta k_{el,i}{}^{k} = k_{el,i}{}^{k-1} \cdot \frac{\Delta ID_j{}^{k}}{\overline{ID}} \tag{2}$$

The iterations are repeated until all ID values ($ID_{EQ1,j}$) are close enough to the target value $\overline{ID}$ (within an acceptable tolerance, for instance $\left|\Delta ID_j\right| \le 0.05 \cdot \overline{ID}$).

The final value of stiffness for each linear spring obtained at the end of the iterative procedure $k_{el,i}$ is then set equal to the initial lateral stiffness of the corresponding CSB:

$$\overline{k_{IN,i}} = \lambda_{1i} \cdot k_{el,i} \tag{3}$$

λ_{1i} is a modification factor accounting for several factors that cannot be captured by the proposed calibration procedure, such as P-Δ effects.

The elongations and the axial forces of each spring under the earthquake design level EQ1 allows to identify the performance point *PP*1.

3.4. STEP 3: Yielding strength and point PP2

The target structural performance associated to PO2 consists ideally in the simultaneous plasticization of the CSBs under the occasional earthquake design level EQ2. It is imposed by calibrating the yielding point of each CSB with numerical simulations (no iterations are required). In detail, once the

initial stiffness values of each linear elastic spring modelling each CSB device have been determined (STEP 2), it is possible to evaluate the peak force in each spring under the earthquake design level EQ2. For this aim, linear time-history analyses are performed on the FE model with the final linear springs and considering an ensemble of ground motions compatible with the EQ2 design level.

The target yielding strength of the i-th CSB ($\overline{F_{yi}}$) is then set equal to the average (over the ground motions ensemble) peak elastic force of the corresponding equivalent linear spring:

$$\overline{F_{y,i}} = \lambda_{2i} \cdot F_{el,i} \tag{4}$$

λ_{2i} is a modification factor accounting for several factors that cannot be captured by the proposed procedure, such as P-Δ effects.

The corresponding target yielding displacement can be then estimated as $\overline{u_{y_i}} = \overline{F_{yi}} / \overline{k_{INi}}$. The values of target yielding displacement and target yielding strength identify the target yielding point *PP*2 of the target capacity curve of each CSB.

3.5. STEP 4: Ductility and point PP3

The target structural performance associated to PO3 consists in the imposition of a uniform ductility demand for all CSBs (that are designed to have consequently larger ductility capacity) in order to ensure an "almost" uniform peak ID profile under the rare earthquake design level EQ3. In the preliminary design phase, it is typical to assume the use of the equal displacement rule for linear and non-linear systems (see [41]), thus allowing to estimate the minimum ductility demand as the ratio between the ordinates of the EQ3 and EQ2 elastic pseudo-acceleration spectra at the fundamental period of vibration, assumed that the latter does not change from EQ2 to EQ3. Then, if the same spectral shape is assumed for the EQ3 and EQ2 response spectra, the ratio between the ordinates of the elastic pseudo-acceleration spectra is coincident with the ratio of the EQ3 and EQ2 peak ground accelerations $a_{g,EQ3}$ and $a_{g,EQ2}$, respectively. According to these simplifications, the ductility demand for the *i*-th CSB can be estimated as: $\overline{\mu}_i = \lambda_{3i} \cdot a_{g,EQ3} / a_{g,EQ2}$. λ_{3i} is a modification factor (typically larger or equal to 1.0) that can be selected by the designer to address special requirements and/or to achieve higher safety levels. λ_{3i} represents a measure of the desired capacity/demand ratio which is imposed for each CSB. In case λ_{3i} values are set larger than 1.0, the structure will be able to resist earthquake intensities higher than EQ3 with the CSBs still in their pseudo-plastic range. The target ductility $\overline{\mu}_i$ allows to identify the potential locations of the performance points *PP*3 (see the orange

dots in Figure 6). The specific location of *PP*3 is then evaluated after the P-Δ effects are approximately evaluated in STEP 5.

3.6. STEP 5: Final hardening and point PP4

The target structural performance associated to PO4 consists in ensuring a minimum strength and displacement capacity for each CSB in order to preserve the global structural stability under the very-rare earthquake design level EQ4. In the preliminary design phase, the global structural stability can be approximately evaluated in terms of second order effects according to the well-known P-Δ method [42,43]. In detail, the frame stability is ensured if the CSBs at the *j*-th storey are able to guarantee an hardening strength $\overline{\Delta F_{h\,j}} = \Delta V_j - \Delta V_{j-1}$, with $\Delta V_j = P_j \cdot \lambda_{4\,j} \cdot \delta_{EQ4} / H_j$ equal to the fictitious shear necessary to balance the *P-Δ* effects. $P_j = \sum_{k=j}^{M} R_k$ is the vertical load acting at the bottom of each column at the *j*-th storey obtained as the sum of the floor loads R_k, while *M* indicates the total number of storeys. δ_{EQ4} is the peak ID demand as obtained from EQ4 earthquake design level. H_j is the *j*-th inter-storey height. At each *j*-th storey, the peak inter-storey displacement δ_{EQ4} can be estimated as $\delta_{EQ4,\,j} = \overline{ID} \cdot H_j \cdot a_{g,4} / a_{g,1}$.

The strength and displacement capacity of the *i*-th CSB can be estimated using the following equations:

$$\overline{u_{h\,i}} = \lambda_{4i} \cdot \delta_{EQ4,\,j} \cdot \cos\vartheta \tag{5}$$

$$\overline{F_{h\,i}} = \overline{F_{yi}} + \left(\overline{\Delta F_{h\,j}} \,/ \cos\vartheta\right) \tag{6}$$

λ_{4i} is a modification factor (typically larger or equal to 1.0) that can be selected by the designer based on specific design requirements and/or safety levels. In case λ_{4i} values are set larger than 1.0, the structure will be able to resist to earthquake intensities higher than EQ4 with the CSBs still in their pseudo-plastic range. On the other hand, larger values of λ_{4i} may lead to large residual displacements. The couple of values $\overline{u_{h\,i}}$ and $\overline{F_{h\,i}}$ identifies the target point *PP*4 of the target capacity curve of each CSB.

3.7. STEP 6: CSB sizing

Once the target mechanical parameters have been obtained (phase B), the CSBs are sized and modelled (phase C). The sizing of each CSB device (assuming the bilinear symmetric configuration displayed in Figure 2) consists in: (i) evaluating the normalized lever arm ξ_0 and cross-section parameters *h* and *J*, leading to the target values of the mechanical parameters for each CSB (i.e. initial stiffness $\overline{k_{IN}}$, yielding strength $\overline{F_y}$ and ductility demand $\overline{\mu}$), and (ii) verifying the actual capacity against P-Δ effects ($\overline{F_h}$, $\overline{d_h}$). Note that both evaluation (i) and verification (ii) can be carried out using the design equations discussed in the Appendix.

3.8. STEP 7: Final verification

Numerical simulations should be carried out by means of non-linear static (pushover) and non-linear dynamic (time-history) analyses considering the actual non-linear characteristics of all structural members and the CSBs as obtained from the preliminary design. The results can be used for the final fine-tuning of the CSBs (slight modifications in geometry and/or cross-section) and to verify all the structural requirements according to code prescriptions.

4. Applicative example

4.1. The analyzed structure

A fictitious 10-storey steel structure is here considered as an applicative example representative of a flexible mid-rise building. The building is supposed to be located in a high seismic risk region of Southern Italy. It has a rectangular plan (30 m x 15 m) with a regular structural mesh (6.00 m along X direction and 5.00 m along Y direction), and a constant inter-storey height *H* equal to 3.5 m for a total height H_{tot} = 35 m. Figure 7 provides a plan view and two elevation views (one unbraced bay and one braced bay). The total vertical load per unit area is equal to 8.0 kN/m^2. The horizontal floors are assumed rigid in their own plane thanks to the presence of stiff diagonal braces.

The vertical resisting system is made by NMRFs composed by columns and beams having European HE and IPE cross-section profiles, respectively, as shown in Figure 7b.

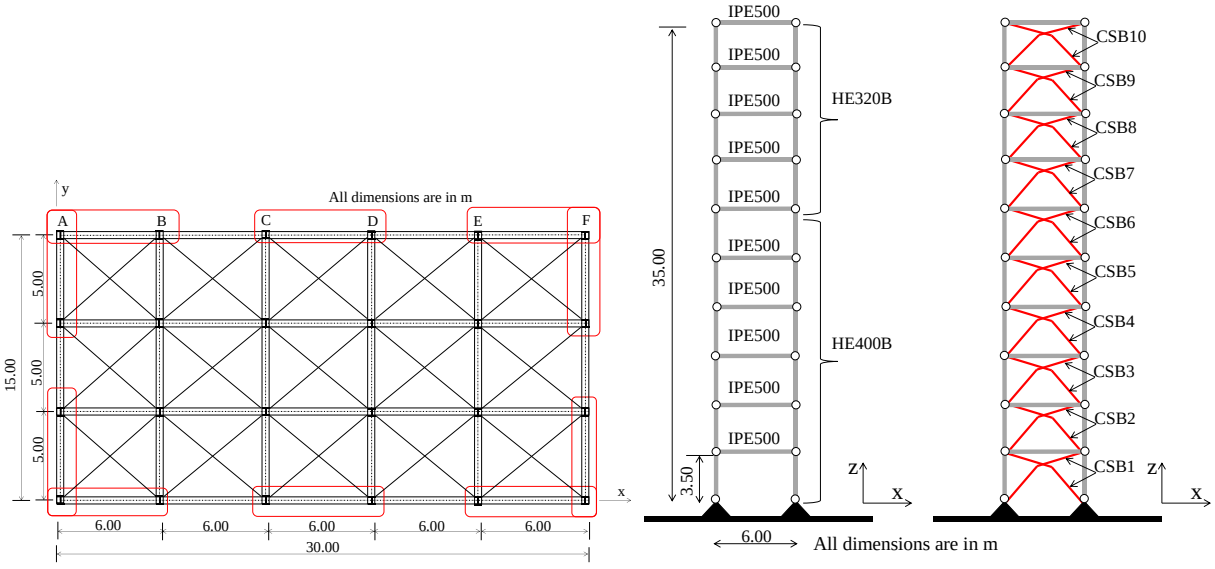

(a) (b) (c)

Figure 7: (a) Plan view of the example building with indication of the braced bays (circled in red). (b) Elevation view of one unbraced bay with indication of the profiles for beams and columns. (c) Elevation view of one braced bay with indication of the CSBs.

Braces are supposed to be inserted in the perimeter frames circled in red in Figure 7a (6 bays along the *y* direction and 4 bays along the *x* direction). For illustrative purposes, the design procedure is here fully developed with reference to one single braced frame along the *y* direction whose elevation view is shown in Figure 7c.

It is assumed to place two equal CSBs at each storey as shown in Figure 7c. Steel grade S235 is considered (elastic modulus E=200 GPa, yielding stress f_y=235 MPa, ultimate stress f_u=360 MPa and ultimate strain ε_u=13.4%).

4.2. Preliminary design of the Uniform CSBF

4.2.1. The linear Finite Element model

The finite element models of the planar frame are developed using the commercial software SAP2000 v18 [44]. All beams and columns are modelled as linear-elastic frame elements with end releases at both end nodes. Different modelling techniques have been employed for the CSBs, following the general procedure presented in the previous section. In particular, for the preliminary design phase, the CSBs are modelled through equivalent linear elastic springs as employed in STEP 2 and STEP 3 to calibrate the initial stiffness and the yielding strength of each CSB.

4.2.2. Earthquake input and performance objectives (STEP 1)

The seismic hazard parameters of the four considered earthquake design levels (EQ1, EQ2, EQ3 and EQ4) are listed in Table 2. They are representative of the city of Reggio Calabria (Southern Italy) characterized by a high seismic hazard level. For each considered earthquake design level, an ensemble of 10 artificial accelerograms has been generated by using SIMQKE software [45]. The resulting average pseudo-acceleration response spectrum with 5% damping ratio is compatible with the design elastic response spectrum as given by the Italian building code [46].

Table 2: Values of the seismic hazard parameters for each earthquake design level.

	T_R [years]	**a_g [g]**	**F_0 [-]**	**T_C^* [s]**
EQ1	60	0.1	2.289	0.295
EQ2	101	0.130	2.300	0.310
EQ3	949	0.359	2.410	0.389
EQ4	1950	0.469	2.469	0.427

The symbols used in Table 2 refer to the seismic hazard parameters as per the Italian building code NTC18 [46]: T_R is the return period, a_g is the ground acceleration on stiff soil (e.g. soil type A); F_0 is the maximum dynamic amplification at the plateau region of the elastic pseudo-acceleration design spectra with 5% damping ratio; T_C^* is a reference value to be used to determine the corner period. The elastic pseudo-acceleration design spectra with 5% damping ratio corresponding to the four design earthquake levels are displayed in Figure 8a. Figure 8b displays the pseudo-acceleration spectra (with 5% damping ratio) of the 10 artificial earthquakes of the EQ1 ground motions ensemble (the red line corresponds to the mean spectrum). The spectra of the other three ensembles have similar shapes and variabilities; therefore, for the sake of conciseness, they are not reported here.

It is worth pointing out that more refined criteria could be used for the selection of ground motion records, such as those based on the conditional spectrum [47], those based on the concept of non-frequent real ground motion records accounting for both record-to-record variability and event-to-event variability [48–50], and those based on the combined use of peak ground motion parameters, such as PGA, PGV and PGD [51]. However, the discussion on selection criteria for the seismic records is beyond the objective of the current work.

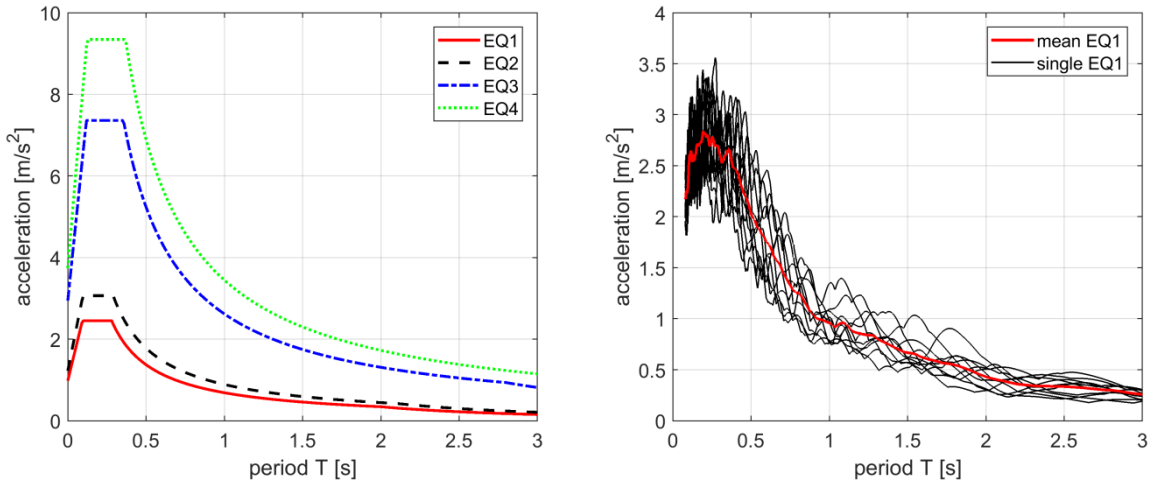

(a) (b)

Figure 8: (a) Elastic design pseudo-acceleration spectra corresponding to the four earthquake intensity levels. (b) Elastic pseudo-acceleration spectra (5% damping ratio) of the ten accelerograms composing the EQ1 ensemble.

The performance objectives, the target mechanical parameters and the modification factors adopted in the applicative example are listed in Table 3.

Table 3: Performance objectives, target mechanical parameters and modification factors

	Performance Objectives	**Target mechanical parameters**	**Modification factors**
PO1	$\overline{ID}$ =0.5% at all storeys under EQ1	$\bar{k}$ from Eqs. (1), (2), (3)	λ_{1i} =1.0
PO2	CSB yielding under EQ2	$\overline{F_y}$ from Eq. (4)	λ_{2i} =1.0
PO3	ductile behaviour under EQ3	$\overline{\mu}$ >3 for all CSBs	λ_{3i} =1.1
PO4	no collapse under EQ4	$\overline{u_h}$ from Eq. (5) $\overline{\Delta F_h}$ from Eq. (6)	λ_{4i} =1.1

4.2.3. Imposition of the target mechanical parameters of the CSBs (STEPS 2-5)

A target ID ratio $\overline{ID}$= 0.5% has been assumed to determine the initial stiffness of the CSBs, as reported in Table 3. At the beginning, a uniform along-the-height initial stiffness value $k_{IN}{}^0$=1 kN/mm is assumed for the 10 linear springs modelling the CSB at all storeys (indicated as S1, S2, …, S10 in

Figure 9a). It is worth noticing that the value of k_{IN}^0 = 1 kN/mm has been selected merely to show the fast convergence of the procedure even in the case of initial peak ID values quite far from the target one. In a more practical case, the initial values of the spring stiffness k_{IN}^0 can be evaluated based on a preliminary structural analysis (for example, through an equivalent static analysis with horizontal forces).

The lateral deformed shape obtained from a linear static analysis with application of a uniform distribution of lateral static forces is represented in Figure 9b. It can be noted that the along-the-height displacement profile is far from being linear.

At the first iteration of the procedure performed to obtain the target initial lateral stiffness, the average peak ID profile has been computed from the linear time-history analyses considering the EQ1 ground motions ensemble (Figure 9c). Also, in this case the peak ID profile is far from being uniform. It should additionally be noted that almost all values (excluding the one at the top storey) exceed the target $\overline{ID}$. This indicates that the initial stiffness of the linear springs k_{IN}^0 is smaller than the one required to satisfy the first performance objective PO1. Thus, in order to satisfy PO1, the iterative procedure described in Section 3.2 has been implemented.

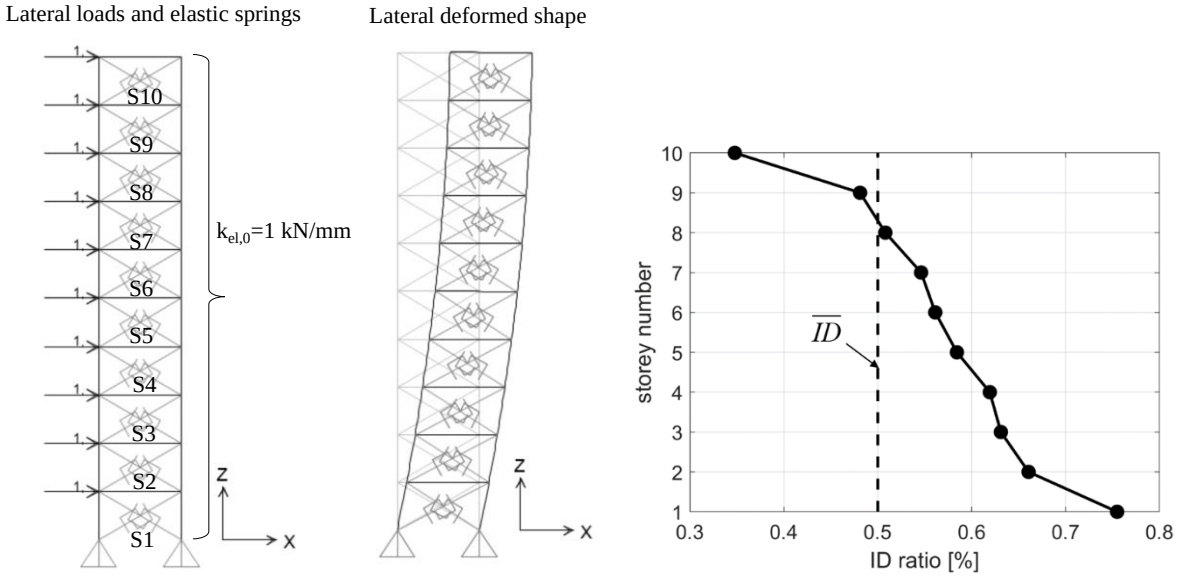

(a) (b) (c)

Figure 9: (a) Uniform distribution of lateral forces for the initial uniform distribution of linear springs. (b) Lateral deformed shape under uniform distribution of lateral forces. (c) Average ID profile under EQ1 design level obtained for the initial uniform distribution of linear springs.

Figure 10a displays the evolution of the average peak ID profiles under EQ1 ground motions ensemble as obtained from the iterative procedure. It can be noted that the values of the final ID rations (red thick curve) reported are within the grey area indicating the target value with a tolerance

of +-10%. Figure 10b displays the updated stiffness values of the linear springs modelling the CSBs located at each iteration. At the end of the iterations, the final stiffness value of each linear spring is set equal to the initial lateral stiffness of the corresponding CSB. Their numerical values are reported in Table 4. As expected, the values increase from the top to the bottom of the frame.

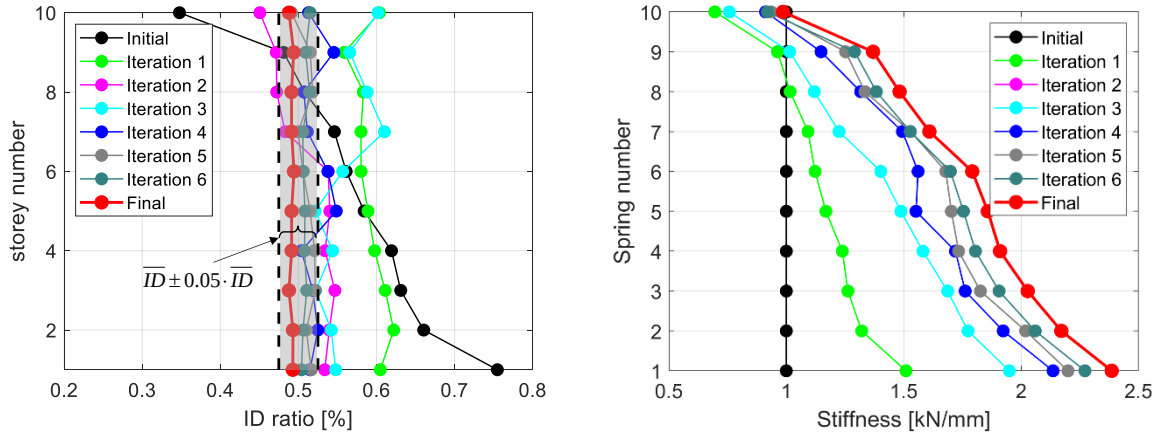

(a) (b)

Figure 10: (a) Average peak ID ratio profile under EQ1 ground motions ensemble. (b) Values of spring stiffness k_{el} at each iteration.

Figure 11a displays the average along-the-height profile of the internal forces in each linear spring as obtained from the linear time-history analyses considering the ground motions ensemble EQ2. Those values are then set equal to the yielding forces of the corresponding CSB. Their numerical values are reported in Table 4.

The fundamental period of vibration of the linear finite element model at the end of the calibration is equal to 6.0 s, while at the initial stage (initial configuration with uniform stiffness at all storeys) it was equal to 8.5 s. It is worth pointing out that the obtained value of the fundamental period is not usual for mid-rise 10-storey steel structures (which are typically characterized by fundamental period values in the range 1.0 – 2.0 s). Rather it corresponds to the typical fundamental period of a much taller and flexible building. This result comes directly from the imposition of uniform 0.5% interstorey drift ratio at PO1. The high flexibility of the fully pinned structure requires a check of the non-linear geometric effects, which will be performed in the final verification step through the simplified P-Δ analysis. However, in practical applications, the structural designer may decide to obtain a stiffer structure with shorter fundamental period by imposing a smaller target ID ratio.

Figure 11b provides the corresponding average peak ID profiles. As expected, the profile is almost uniform with maximum values increased of a factor of around 1.27 with respect to those obtained

considering the ground motion EQ1 ensemble. This value is close to the ratio $a_{g,EQ2}/a_{g,EQ1}$ (namely, the ratio between the peak ground accelerations of the EQ2 design level and the EQ1 design level).

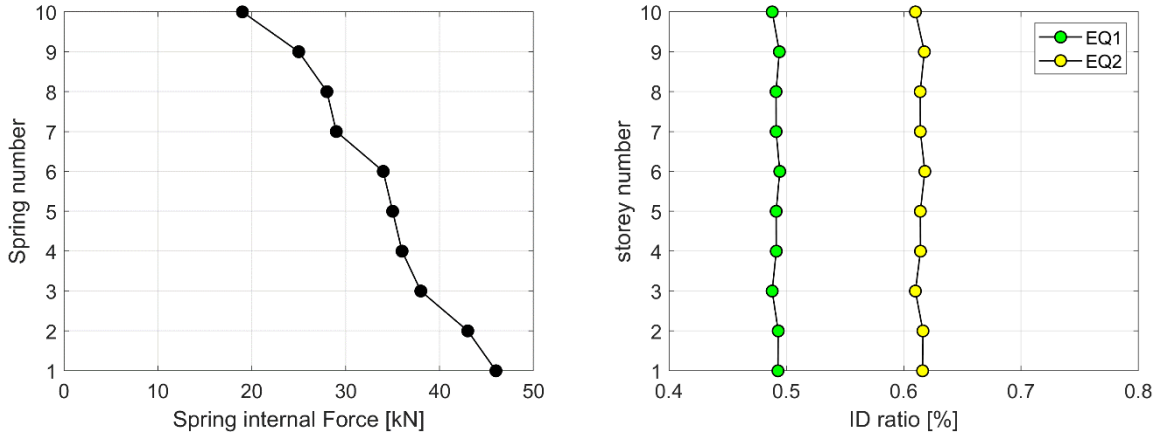

(a) (b)

Figure 11: (a) Peak axial forces in the linear diagonal springs under the EQ2 design level. (b) Average peak *ID* ratio profile under the EQ2 ground motions ensemble.

The target displacement ductility demand $\bar{\mu}$ is evaluated considering a coefficient λ_{3i} = 1.1 and the values of $a_{g,EQ3}$ and $a_{g,EQ2}$ as reported in Table 2. The over-strength and displacement capacities of each CSB to prevent collapse induced by P-Δ effects are evaluated considering a coefficient λ_{4i} = 1.1 and the values of $a_{g,EQ4}$ and $a_{g,EQ1}$ as reported in Table 2. The numerical values of $\bar{\mu}$, $\overline{\Delta F_{P-\Delta}}$ and $\overline{u_{P-\Delta}}$ are collected in Table 4.

4.2.4. CSB sizing (STEP 6)

The CSBs are sized according to the direct design equations reported in the Appendix making use of the values of $\overline{k_{IN}}$, $\overline{F_y}$ and $\bar{\mu}$, $\overline{\Delta F_{P-\Delta}}$, $\overline{u_{P-\Delta}}$ as reported in Table 4. The values of $\overline{\xi_0}$, $\bar{h}$ and $\bar{J}$, calculated using the direct design equations, are also reported in Table 4.

The cross-section profiles of the CSBs have been selected as tubular circular profiles that have the closest geometrical parameters as the target ones. For each CSB, the values of the actual normalized lever arms ξ_0, cross-section external diameter (*D*), moments of inertia (*J*) and thickness (*t*) are provided in Table 4.

Table 4: Target mechanical parameters, target cross section parameters and actual cross section parameters for each CSB.

CSB number	Target mechanical parameters (from Eqs. 1-6)					Target cross-section parameters (from Eqs. A4-A6)			Actual cross-section parameters			
	$\overline{k_{in}}$ [kN/mm]	$\overline{F_y}$ [kN]	$\overline{\mu}$	$\overline{\Delta F_h}$ [kN]	$\overline{u_h}$ [mm]	$\overline{\xi_0}$ [%]	$\overline{h}$ [mm]	$\overline{J}$ [mm4]	ξ_0 [%]	D [mm]	t [mm]	J [mm4]
CSB1	2.46	45.64	3.0	9.3	75	8.0	191	$8.26 \cdot 10^6$	8.0	195	3.0	$8.34 \cdot 10^6$
CSB2	2.31	42.58	3.0	9.3	75	7.9	192	$7.74 \cdot 10^6$	8.0	190	3.0	$7.71 \cdot 10^6$
CSB3	2.12	38.44	3.0	9.3	75	7.9	194	$7.02 \cdot 10^6$	8.0	190	3.0	$7.71 \cdot 10^6$
CSB4	1.97	35.80	3.0	9.3	75	7.9	194	$6.53 \cdot 10^6$	8.0	190	2.5	$6.47 \cdot 10^6$
CSB5	1.93	34.83	3.0	9.3	75	7.9	195	$6.38 \cdot 10^6$	8.0	190	2.5	$6.47 \cdot 10^6$
CSB6	1.88	33.95	3.0	9.3	75	7.9	195	$6.22 \cdot 10^6$	8.0	190	2.5	$6.47 \cdot 10^6$
CSB7	1.65	29.45	3.0	9.3	75	7.8	196	$5.41 \cdot 10^6$	8.0	190	2	$5.22 \cdot 10^6$
CSB8	1.55	27.62	3.0	9.3	75	7.8	196	$5.08 \cdot 10^6$	8.0	190	2	$5.22 \cdot 10^6$
CSB9	1.43	25.43	3.0	9.3	75	7.8	196	$4.68 \cdot 10^6$	8.0	190	2	$5.22 \cdot 10^6$
CSB10	1.08	19.12	3.0	9.3	75	7.8	197	$3.58 \cdot 10^6$	8.0	190	1.5	$3.94 \cdot 10^6$

Clearly, the real geometrical parameters of the sized CSBs results in slightly different mechanical performances from the target ones. To evaluate the level of approximation related to these slight discrepancies, the full non-linear force-displacement capacity curves of the CSBs have been obtained from numerical simulations carried out using the Finite Element software SeismoStruct [52]. Each straight segment of the CSB was modelled with a fiber beam element using the force-based formulation [53]. Non-linear geometry was approached using the corotational formulation [54]. Material non-linearity was considered using the Menegotto–Pinto law with the isotropic hardening introduced by Filippou et al. [55] to model the experimental hysteretic behavior of the steel. It has been shown [33] that such modelling technique allows to accurately reproduce the experimental non-linear response of the CSBs. Figure 12 displays the force-displacement capacity curves of three selected CSBs (CSB1, CSB5 and CSB10). The force-displacement curves are obtained by performing non-linear static analysis by imposing a lateral displacement *d* as sketched in Figure 12a. In particular, Figure 12b provides the zoom for low values of forces and displacements, in order to compare the actual non-linear curves of the three CSBs with the target initial lateral stiffness (dotted straight lines) and yielding point (full circular dots). It can be noted that the level of approximation is acceptable for preliminary design purposes.

In the next section the implications of these approximations are further assessed through non-linear static and dynamic analyses performed on the whole braced frame.

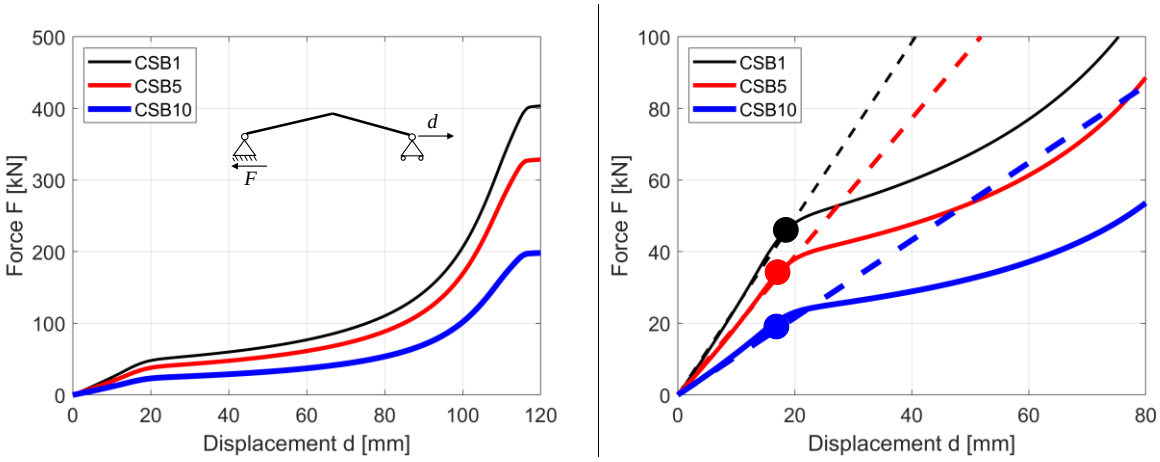

Figure 12: (a) Full force-displacement responses of three selected CSBs; (b) Zoom of the force-displacement responses of three selected CSBs as compared with the target initial stiffness and yielding point.

4.3. Final verifications through non-linear numerical simulations (STEP 7) and comparison with the performances of a conventionally braced structure

4.3.1. The non-linear Finite Element Analysis

The final verifications are carried out through non-linear Finite Element Analysis (FEA) developed with the commercial software SAP2000 v18 [44]. The purpose of the numerical analyses is twofold: (1) to evaluate the actual seismic performances of the Uniform CSBF, (2) to compare the performances of the CSBF with those of a CBF characterized by the same initial storey stiffness values.

For the first aim, a non-linear FE model of the CSBF has been established. Each straight segment of the CSB is modelled through two non-linear beam elements with plastic hinges (uncoupled flexural and axial) placed at both end nodes. Steel grade S235 is considered (yielding strength equal to f_y=235 MPa and elastic modulus equal to E=210000 MPa). The inherent damping value of 5% (typical for steel structures) is assumed. The normalized backbone curves describing the behavior of the flexural plastic hinges (bending moment-curvature) and axial plastic hinges (axial force-axial elongation) are provided in Figure 13. The backbone curves are obtained considering an elastic-perfectly plastic material behavior and are normalized with respect to yielding values.

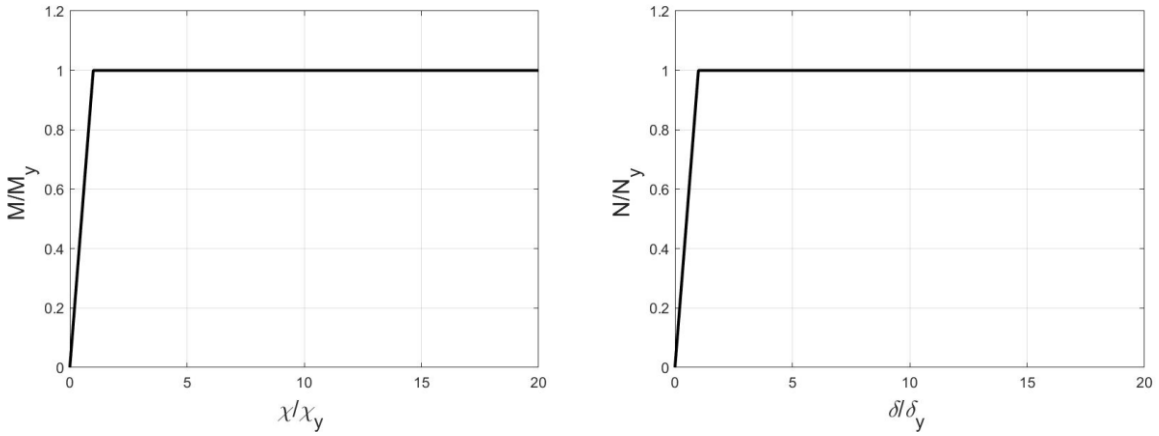

(a) (b)

Figure 13: Normalized backbone curves for the (a) flexural and (b) axial plastic hinges of the CSBs (*abs* values are limited to 20).

The fundamental period of the CSBF model is equal to 6.3 s. It should be noted that the slight difference between the fundamental periods of the linear and non-linear CSBF models is due to the slight differences between the target and the actual values of the main geometrical properties of the CSBs, as summarized in Table 4.

For the second aim, a non-linear FE model of the frame equipped with conventional diagonal frames (CBF) has been established. It should be noted that, in the sizing of the diagonal braces of the CBF model, the compressed braces (characterized by very large slenderness values) have been ignored, given their negligible contribution in compression due to premature buckling failure. Consequently, the (full circular) cross-section area of each diagonal brace in tension is calculated by assuming an axial stiffness coincident with the target initial stiffness of the couple of CSBs of the corresponding storey (e.g. $\overline{k_{CB}} = 2 \cdot \overline{k_{IN}}$). Table 5 provides the numerical values of the target axial stiffness $\overline{k_{CB}}$ of each CB together with the values of the actual diameters D_{CB}. Steel grade S235 is considered, along with the same properties adopted for the CSBs. In the FE model the CBs are modelled as non-linear truss elements with axial plastic hinges at both end nodes.

Table 5: Target mechanical parameters, target cross section parameters and actual cross section parameters for each CB.

CB number	**Target mechanical parameter**	**Target cross-section parameter**	**Actual diameter of the full circular cross-section**
	$\overline{k_{CB}}$ [kN/mm]	$\overline{A_{CB}}$ [mm^2]	D_{CB} [mm]

CB1	4.91	170.59	14.7
CB2	4.63	160.73	14.3
CB3	4.24	147.12	13.7
CB4	3.94	136.78	13.20
CB5	3.86	134.18	13.1
CB6	3.77	130.89	12.9
CB7	3.30	114.70	12.08
CB8	3.10	107.73	11.7
CB9	2.86	99.29	11.24
CB10	2.16	75.01	9.8

A linear along-the-height profile of the external lateral forces (Figure 13a) is adopted for the non-linear static (pushover) analysis, while the four ground motion ensembles described in Section 4.2.2 are used for the non-linear dynamic time-history analyses.

Concentrated vertical forces of 150 kN were applied at the top of each column to account for the P-Δ effects. All non-linear analyses were carried out considering both the mechanical non linearities (plastic hinges) and the geometrical non-linearities (according to the formulations implemented in SAP2000 considering *"P-Δ"* and *"large displacements"*, see [44]).

It should be noted that the obtained numerical results are always affected by model (epistemic) uncertainties that lead to unavoidable discrepancies between the theoretical predictions, either analytical or numerical, and the actual response of the structure (especially in the case of non-linear models, see e.g. [56]) which hence should be considered in design applications.

4.3.2. Results from non-linear static analyses

4.3.2.1.Comparing CSBF and CBF models ignoring P-Δ effects

The non-linear static (pushover) analyses have been first carried by applying the linear along-the-height profile of lateral forces only, thus ignoring the concentrated vertical loads.

The comparison of the resulting capacity curves and the representation of the evolution of the activation of the plastic hinges for the CSBF and CBF models is displayed in Figure 14.

Figure 14a refers to the CSBF model. The activation of the plastic hinges is represented with green dots, while the corresponding events in the pushover curve are indicated with red dots and capital letters. It can be noted that the flexural plastic hinges at the knee cross-section of the CSBs progressively activate along the whole height starting from the lower storeys and then involving the upper ones. The first plastic hinges (point A) activate at the first four fourth stories almost simultaneously for a base shear within 70-90 kN and a roof displacement within 200-210 mm. Then,

plastic hinges appear almost simultaneously to all the CSBs up to the sixth storey (points B, C). The remaining flexural plastic hinges (points B, C, D) activate at the higher stories up to point D reaching a roof displacement of 600 mm and a base shear of 110 kN and a roof displacement of 955 mm at the point F. The final hardening after the pseudo-plastic plateau ends at point E (base shear of 360 kN and roof displacement of 1080 mm) with the axial yielding of the brace at the fourth stories followed by the progressive yielding of the other braces up to point F where the analysis was interrupted (note that the roof displacement of 1200 mm corresponds to a roof drift ratio of roughly 3.5 %). It is important to highlight that the shape of the real capacity curve reflects the expected target one (see Figure 12b), even though the differences between the target and the actual properties of the CSBs do not lead to a perfectly synchronized yielding.

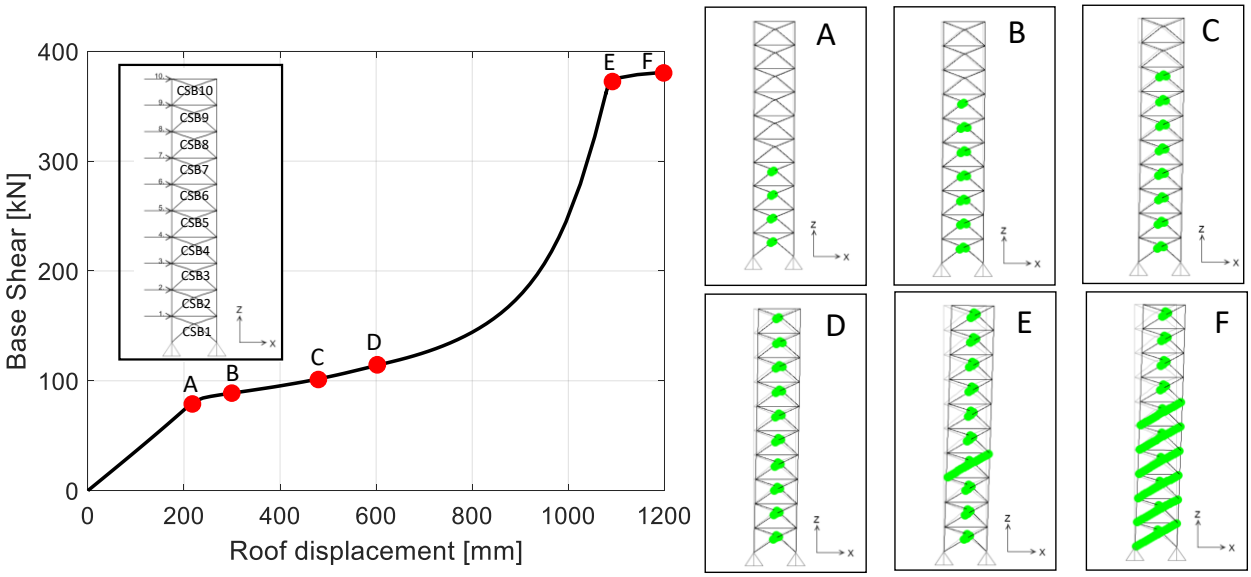

(a)

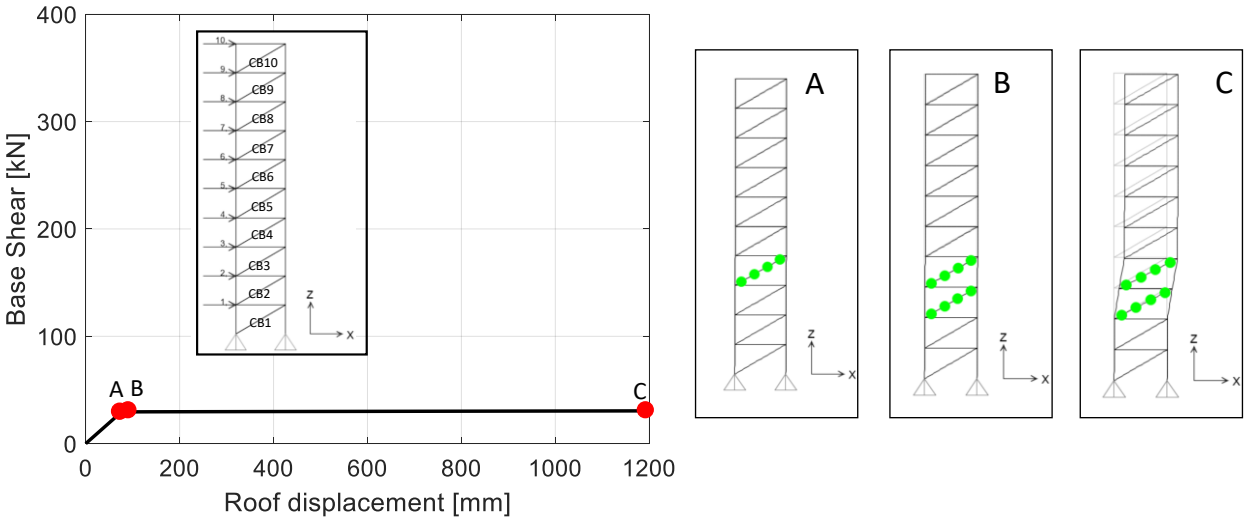

(b)

Figure 14: Pushover curve and plastic hinges activation for: (a) CSBF model. (b) CBF model.

Figure 14b refers to the CBF model, instead. As expected, the pushover curve of the CBF model has the same initial stiffness of that of the CSBF model. The first plastic hinges activate at the fourth and third storey (events A and B, respectively) almost simultaneously for a base shear equal to 30 kN, less than one half of the base shear leading to first yielding for the CSBF model. The second plastic hinges (point B) activate at the fifth storey almost simultaneously to the first storey, then leading to the formation of a kind of soft/weak storey mechanism involving only the fourth and fifth storeys (point C). All the other CBs remain in the elastic field. After reaching point C the analysis was interrupted (roof displacement of 1200 mm).

4.3.2.2.Discussion on the P-Δ effects

The non-linear static (pushover) analysis has been then carried by applying the along-the-height profile of lateral forces together with the concentrated vertical loads to account for the P-Δ effects. The comparison of the resulting capacity curves and the graphical representation of the evolution of the activation of the plastic hinges for the CSBF and CBF models is displayed in Figure 15. For the sake of comparison, also the capacity curves ignoring the P-Δ effects are shown in the figures.

The capacity curve of the CSB model considering the P-Δ effects (Fig. 15a) evidences, as expected, a reduction of the base shear capacity due to the detrimental contribution of the geometric stiffness k_g, while the displacement capacity remained almost unaltered. In fact, despite the unavoidable effect of the reduction of the base shear capacity, the shape of the capacity curve is qualitatively similar to that obtained ignoring the P-Δ effects. This is due to the activation of a similar global mechanisms of collapse involving the flexural yielding of all the CSBs before their axial yielding, thus avoiding the formation of weak/soft stories. The first CSBs yielding (event A) occurs for a base shear of around 60 kN (15% reduction with respect to the capacity ignoring P-D effects). The base shear capacity at the formation of the axial plastic hinges (event E) is equal to 270 (25% reduction with respect to the capacity ignoring P-Δ effects).

The capacity curve of the CBF model considering the P-Δ effects (Fig. 15b) reaches the peak point at event A corresponding to the formation of the first axial plastic hinge for the brace located at the third storey. The base shear capacity results equal to 23 kN (reduction of 23% with respect to the capacity ignoring P-Δ effects). Event A represents the collapse point of the structure since for larger displacement a softening branch due to P-Δ effects is observed. It is thus clear that for the CBF model the capacity is overall strongly reduced since the plastic branch observed for the model without P-Δ effects cannot be developed.

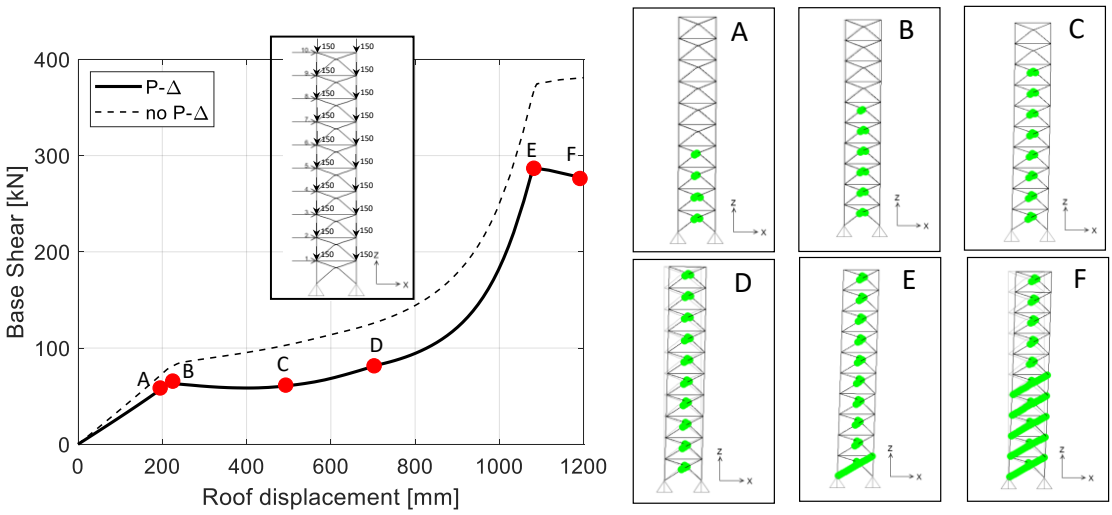
P-Δ
no P-Δ
Base Shear [kN]
Roof displacement [mm]
A
B
C
D
E
F

(a)

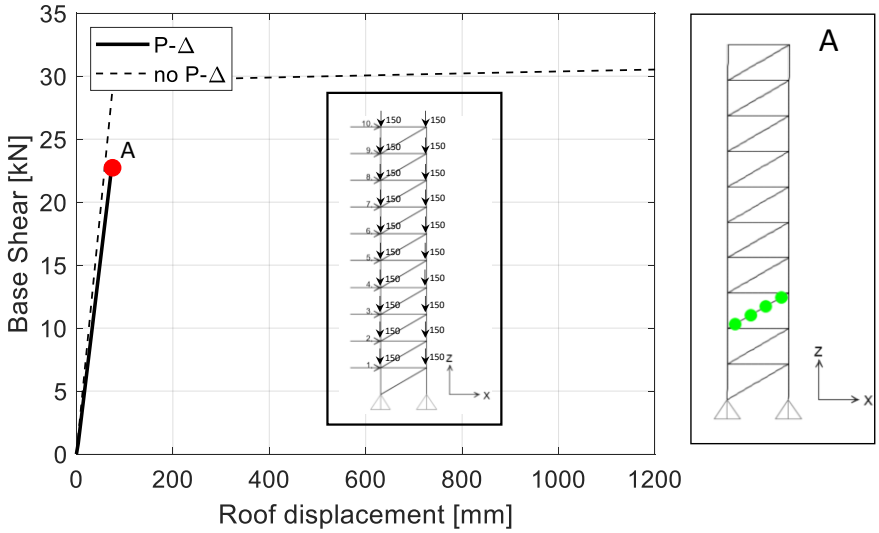
P-Δ
no P-Δ
Base Shear [kN]
Roof displacement [mm]
A

(b)

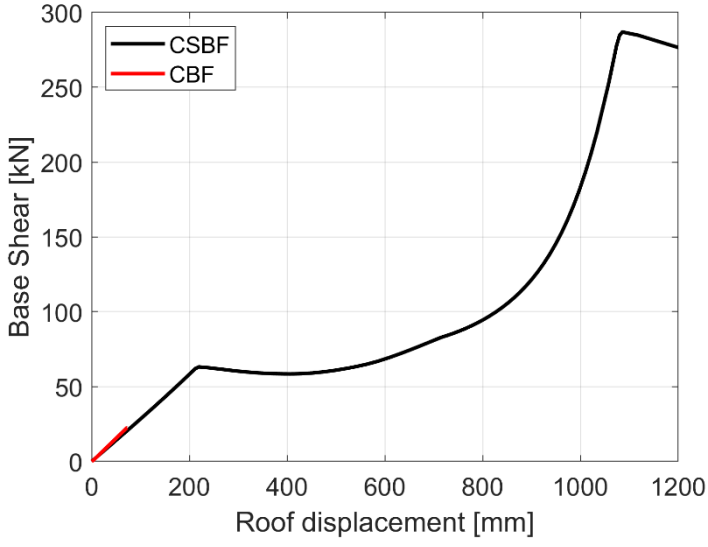
CSBF
CBF
Base Shear [kN]
Roof displacement [mm]

(c)

Figure 15: Pushover curve and plastic hinges activation for: (a) the CSBF model and (b) the CBF model. (c) Comparison of pushover curves for the CSBF and the CBF models.

4.3.3. Results from non-linear dynamic time-history analyses

4.3.3.1.Comparing CSBF and CBF models ignoring P-Δ effects

The non-linear dynamic time-history analyses have been first carried out considering only the effects of the earthquake induced horizontal actions, thus ignoring the *P-Δ* effects. For this aim, the distributed vertical load of 100 kN/m applied to each beam is only considered in terms of horizontal mass source thus neglecting its effect in terms of axial forces in the columns. The main purpose of this analysis is to compare the seismic dynamic response of the CSBF and CBF models with the corresponding capacity curves and assess the residual drifts for the different earthquake intensity levels.

The comparison of the main results obtained from the non-linear time history simulations performed on the CSBF and CBF models are graphically summarized in Figures 16 and 17.

Figure 16a provides a synthetic overview of the global performances under the four earthquake design levels (EQ1, EQ2, EQ3 and EQ4) in terms of base shear vs first peak ID ratio. Each small colored diamond refers to the results of a single time-history analysis (each color corresponds to a different ground motion ensemble), while the big squares provide the corresponding average response (over the ten accelerograms of the same ensemble). The graph includes also the capacity curves obtained from the pushover analysis with the performance points for the CSB frame (PPs) indicated with small colored dots to facilitate the visual comparison between target performance points and average seismic response. It can be noted that the results of the dynamic time history analyses follow the corresponding capacity curve even though some discrepancies are observed. These differences are induced by the well-known effects due to the load patterns of the lateral forces and the nature of the actions (static vs dynamic) on the capacity curve [57,58]. Careful inspection of the graph of Figure 16a allows to draw some interesting observations.

For the CSBF model:

- the average displacement demand in terms of *ID* ratio under EQ1 is equal to the imposed target drift ratio $\overline{ID}$=0.5;
- the average seismic demand under EQ2 (base shear equal to 74 kN and first storey drift ratio equal to *ID*=0.66%) is close to the first yielding point of the capacity curve;
- the average seismic demand under EQ3 (base shear equal to 96 kN and first storey drift ratio equal to *ID*=1.4%) in terms of displacements is almost twice the one observed under EQ2, thus revealing that the actual ductility demand is less than the expected one (set equal to 3.0);

- the average seismic demand under EQ4 (base shear equal to 110 kN and first storey drift ratio equal to *ID*=1.8%) highlights a hardening response even though still within the pseudo-plastic range, thus indicating an extra safety margin against very rare earthquakes.

For the CBF model:

- the average seismic displacement demand under EQ1 and EQ2 is similar to that experienced by the CSBF model, even though the yielding strength of the CB at the first storey was already achieved for EQ1.
- The average seismic displacement demand under EQ3 and EQ4 was significantly higher than the corresponding one exhibited by the CSB model (+ 60% under EQ3 and + 80% under EQ4).

Figure 16b displays the average peak ID profiles corresponding to the four different earthquake design levels. It can be noted the profiles under both EQ1 and EQ2 are almost uniform, even though variations between the values of consecutive storeys are slightly larger than the ones obtained analyzing the elastic FE model with the equivalent linear springs (see Figure 10a). Larger variations are observed when considering EQ3 and EQ4. These variations are mainly related to the discrepancies between the target and actual stiffness and yielding strength of the CSBs that do not allow to obtain a perfectly simultaneous along-the-height yielding.

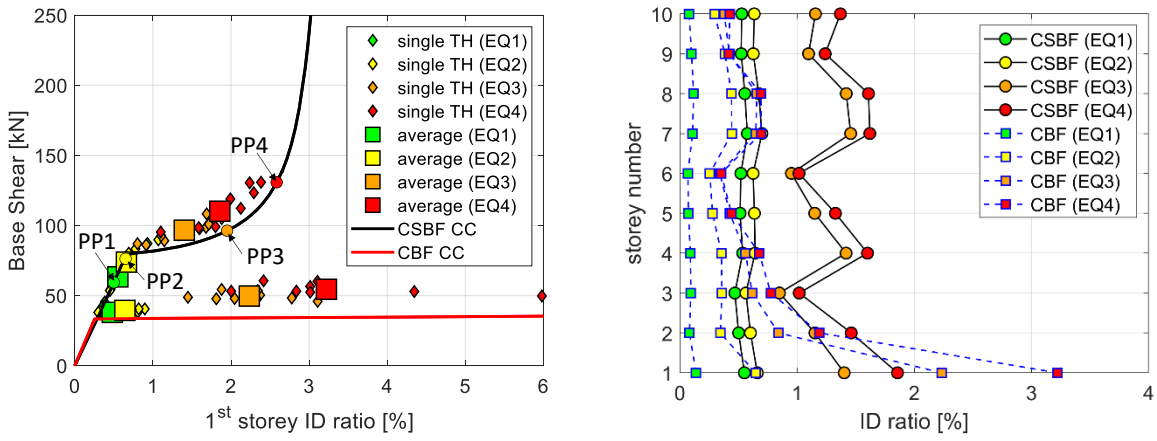

(a) (b)

Figure 16: (a) Average peak seismic response in terms of base shear vs ID ratio. (b) Average peak ID ratio profiles.

Figures 17a, b, c and d provide the bending moment vs plastic rotation responses of the plastic hinges located at the knee points of three selected CSB devices for the CSBF model (namely: CSB1, CSB5 and CSB10) under the most severe accelerogram (in terms of excursion in the plastic field) considering the four EQ levels. Similarly, Figures 18a, b, c and d provide the axial force vs plastic displacement responses of the three corresponding braces for the CBF model under the most severe

accelerogram (in terms of excursion in the plastic field) considering the four EQ levels. First it should be noted that, while for the CSBF model all the CSBs remained within the elastic field for earthquakes of EQ1 ensemble and for all but one earthquakes of EQ2 ensemble, for the CBF model some braces exceeded yielding for all earthquakes.

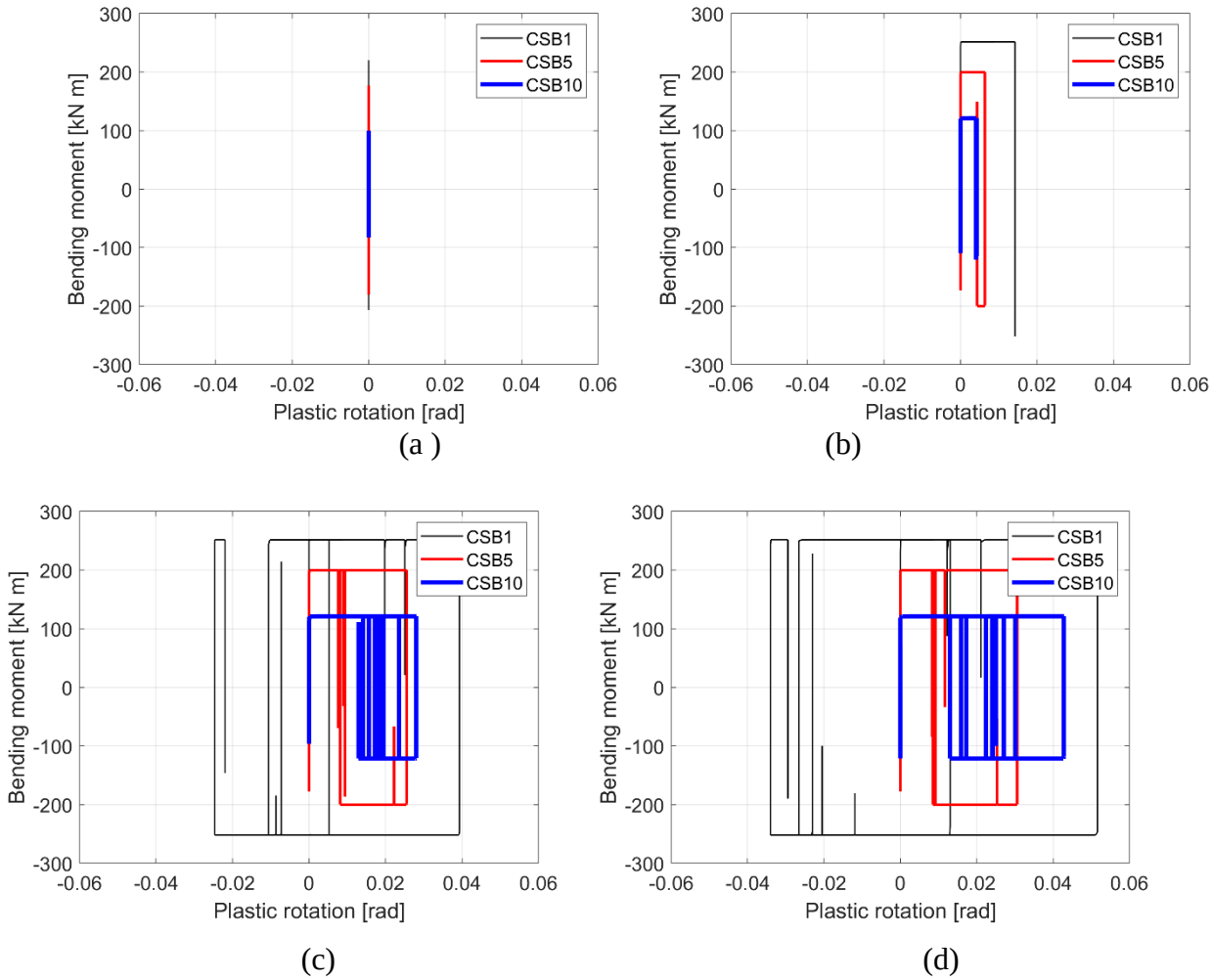

Figure 17: Moment-rotation cyclic response of selected plastic hinges for the most demanding earthquake in terms of inelastic response (a) EQ1 intensity level; (b) EQ2 intensity level; (c) EQ3 intensity level; (d) EQ4 intensity level.

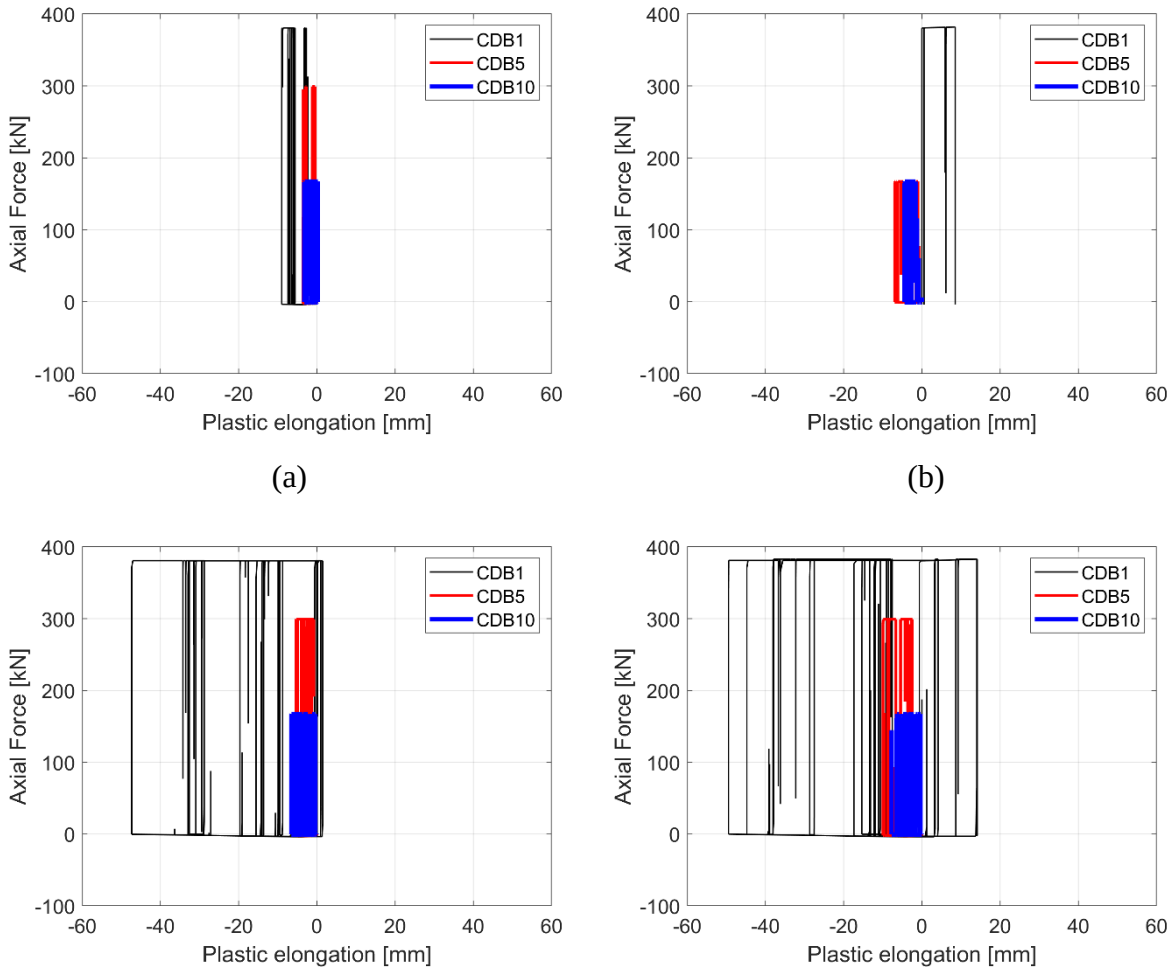

Figure 18: Force-elongation cyclic response of selected plastic hinges for the most demanding earthquake in terms of inelastic response (a) EQ1 intensity level; (b) EQ2 intensity level; (c) EQ3 intensity level; (d) EQ4 intensity level.

The graphs show that, for both earthquake EQ3 and EQ4 design levels, the range of the plastic field increases going from the CSB located at the top storeys to those located at the bottom storeys. This finding appears in line with the results obtained from the pushover analysis.

Figure 19 provides the average along-the-height profiles of the residual ID as evaluated at the last step of the dynamic time-history analyses.

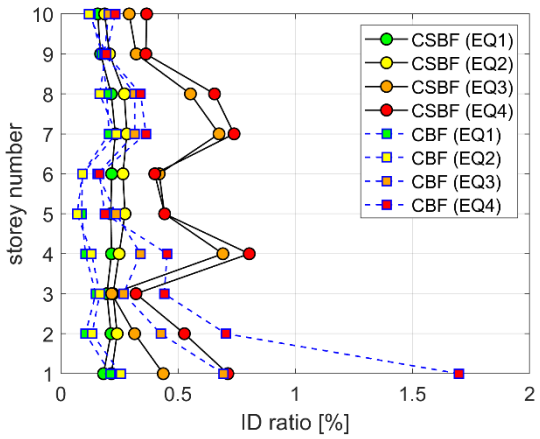

Figure 19: Average Residual ID ratio profiles.

The results presented in this section confirm that the proposed design approach for the Uniform CSBF based on the use of CSBs designed to fulfill multiple seismic performance objectives led to the desired seismic performances. On the contrary, the simple design criterion adopted for the CBF based on a single performance objective, that is limiting the peak ID under EQ1, led, as expected, to not satisfactory seismic performances.

4.3.3.2.Discussion on the P-Δ effects

The non-linear dynamic time-history analyses have been then carried out considering also the effects of the axial loads in the columns by applying the concentrated vertical loads.

It should be first noted that, while the CSBF model was able to sustain all the considered earthquakes of the four EQ levels without experiencing failure, the CBF model was, instead, not able to sustain none of the considered earthquakes at all EQ levels. The collapse occurred due to failure of the CBs leading to a global unstable configuration. For this reason, the discussion of this section is limited to the comparison of the seismic response of the CSBF model with and without consideration of P-Δ effects.

Figures 20a, b, and c summarize the global performances of the CSBF, as obtained through non-linear dynamic time history analyses under the four earthquake design levels (EQ1, EQ2, EQ3 and EQ4) in terms of base shear vs first storey peak ID ratio (Figure 20a), peak ID ratio profiles (Figure 20b) and residual ID ratios profiles (Figure 20c). As expected, Figure 20a shows that the P-Δ effects becomes significant when considering the two highest earthquake intensity levels (namely EQ3 and EQ4) leading two a very large increase in the displacement demand, namely + 114% when considering EQ3 and +88% when considering EQ4. The relatively smaller increase of displacement demand at EQ4 is due to the beneficial effect of the final hardening stiffness of the CSB. Figures 20b and c show that the higher increase in the peak ID values is concentrated at the bottom stories.

As final remark, it is worth noticing that the significant P-Δ effects observed in the presented case study depend mostly on the very high flexibility of the structure, which, as previously highlighted, is more representative of a tall building, rather than of a mid-rise building. Nevertheless, the results of the numerical simulations showed that, even for such a flexible structure, the presence of the CSB was able to lead to acceptable seismic performances.

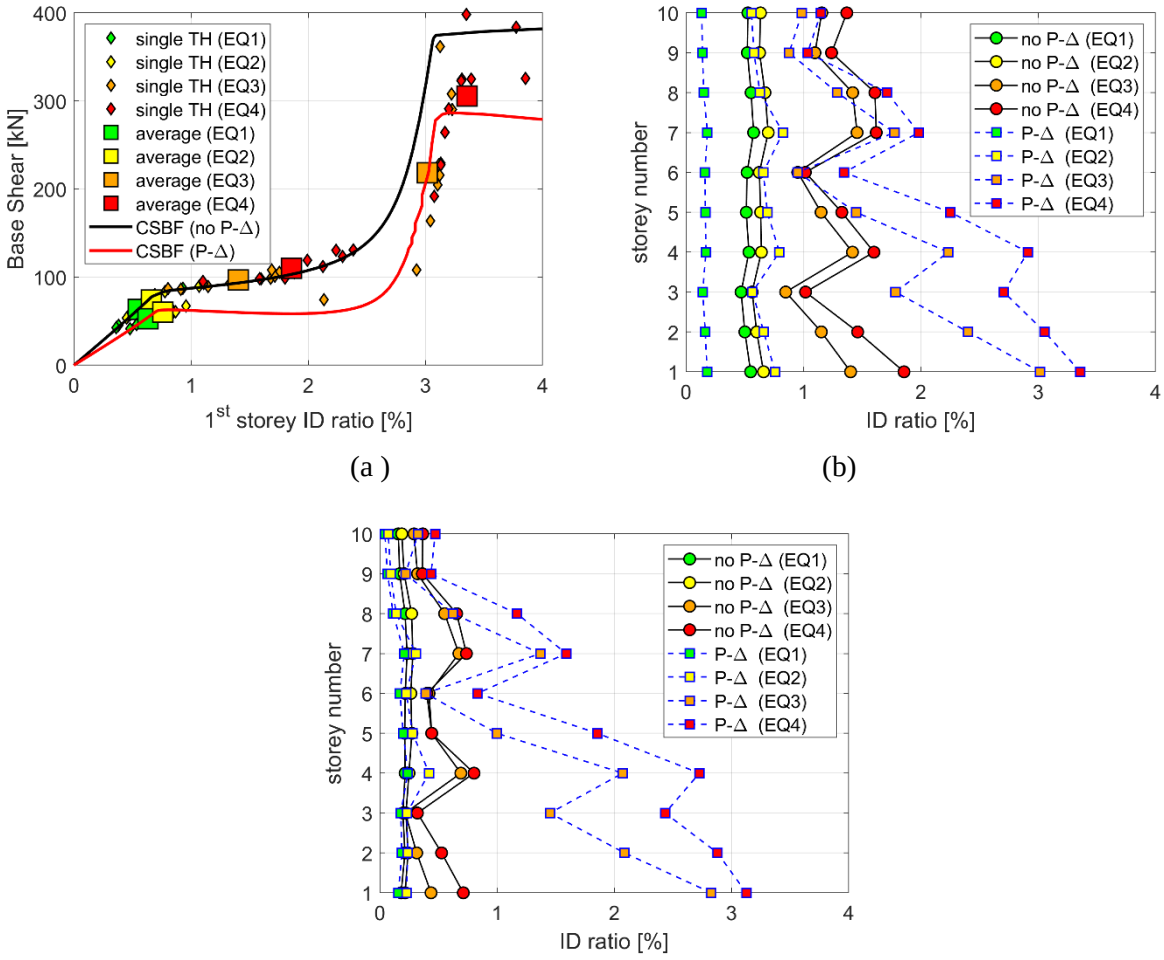

Figure 20: Main results from the dynamic time history analysis for the CSBF model considering the P-D effects: (a) Average peak seismic response in terms of base shear vs ID ratio. (b) Average peak ID ratio profiles. (c) Average Residual ID ratio profiles.

Conclusions

This paper introduces a novel seismic design procedure for mid-rise not moment-resisting frames (NMRF) equipped with special yielding braces called Crescent Shaped Braces (CSBs) capable of satisfying multiple seismic performances within the PBSD framework, to ensure an almost uniform along-the height seismic behaviour. The use of CSBs as enhanced diagonal braces in a NMR frame leads to a novel structural system here defined as CSB Frame (CSBF).

The conceptual design approach behind the proposed design procedure includes four phases, from the preliminary design to the final verifications as follows: (i) definition of the seismic performance objectives for the whole structure (phase A); (ii) evaluation of the target mechanical parameters for each CSB (phase B); (iii) sizing of each CSB (phase C); (iv) final verification of the actual seismic behavior of the whole structure (phase D).

The proposed step-wise design procedure assists the professional engineer through the different design phases with the aim of achieving specific target seismic performances leading to the desired along-the-height seismic behavior. The target seismic performances include: (i) uniform along-the-height peak inter-storey drift profile under frequent earthquakes; (ii) simultaneous yielding of all CSBs along the height under occasional earthquakes; (iii) along-the-height uniform ductility capacity and diffuse plasticization under rare earthquakes; (iv) final hardening stiffness to prevent global collapse due to P-Δ effects under very rare earthquakes.

The steps related to the preliminary design are carried out with simplified linear FE models in which the CSBs are modelled as equivalent linear elastic springs with axial stiffness calibrated (through a simple iterative numerical procedure) to obtain a target uniform along-the-height peak inter-storey drift. The target yielding strengths of the CSBs are then evaluated by imposing their simultaneous yielding under an occasional earthquake intensity. The minimum target ductility capacity of the CSBs is imposed considering a rare earthquake intensity to obtain a diffuse plasticization of the CSBs. The minimum hardening capacity is evaluated by preventing the collapse under P-Δ effects considering a very rare earthquake intensity. Then, simplified direct design equations are used to size the CSBs in order to meet the target mechanical performances. Clearly, the real geometrical properties of the sized CSBs (in terms of global geometry and cross-sections) will lead to an actual seismic behavior which slightly differs from the ideal target one.

The effectiveness of the proposed design procedure has been demonstrated through an applicative example, namely a mid-rise 10-storey steel structure. Two structural systems were compared: the proposed solution (CSBF structure) designed to fulfill the four performance objectives and a conventional solution based on the use of concentric diagonal braces (CBF structure) designed just to fulfill the first performance objectives (uniform peak interstorey drifts under frequent earthquakes). The final verifications were carried out by means of non-linear time history analyses performed either ignoring or considering the geometrical second order effects.

First, it has been shown that the iterative procedure leading to the calibration of the initial stiffness of the CSBs converges in few iterations. Then, it is shown that the direct design equations are accurate enough to size CSBs with actual force-displacement curves close to the target ones. The main findings from the final verifications carried out through non-linear static and dynamic analyses demonstrated

that the slight differences between the target and the actual mechanical performances of the CSBs do not prevent the achievement of the target performance objectives. The final comparisons between the seismic performances of the CSBF and CBF demonstrated the superior performances of the CSBF structure, especially when considering the geometrical second order effects.

Appendix

In the work by Palermo et al. [35], analytical relationships (Eqs. A1-A3) were proposed to estimate the key mechanical properties k_{IN}, F_y and μ in terms of the main geometrical characteristics of the CSB device, i.e. ξ_0, *h* and *J*.

$$k_{IN} = \frac{3}{8} \cdot \frac{E \cdot J \cdot \cos\theta_0}{{L_0}^3 \cdot {\xi_0}^2} \tag{A1}$$

$$F_y = \frac{W_e \cdot f_y}{d_0} \cdot \gamma = \frac{f_y \cdot J}{L_0 \cdot h \cdot \xi_0} \cdot \gamma \tag{A2}$$

$$\mu = \frac{3}{4} \frac{E}{f_y} \frac{h}{L_0} \frac{\left|\left(\cos\theta_{5\%} - \cos\theta_0\right)\right|}{\xi_0 \cdot \gamma} \tag{A3}$$

where $\gamma = \dfrac{1}{1 + \dfrac{h}{2L_0} \cdot \dfrac{2}{\xi_0} \cdot \left(\dfrac{i}{h}\right)^2}$ is a non-dimensional parameter.

With the aim of deriving direct design equations to dimension the CSB device in terms of the target mechanical parameters ($\overline{k_{IN}}$, $\overline{F_y}$ and $\overline{\mu}$), the following assumptions have been made: $5\% \le \xi_0 \le 25\%$, $\gamma = 1$, $\cos\theta_0 = 1$. After simple mathematical manipulations of Eqs. A1-A3, the following analytical relationships can be derived:

$$\xi_0 = \frac{0.06 \cdot \rho + \sqrt{0.014 \cdot \rho^2 + 7.8 \cdot \rho \cdot \overline{\mu}}}{3.9 \cdot \rho} \tag{A4}$$

$$h = \frac{4}{3} \cdot \frac{f_y}{E} \cdot \rho \cdot L_0 \cdot \xi_0 \tag{A5}$$

$$J = \frac{4}{3} \cdot \frac{\overline{F_y}}{E} \cdot \rho \cdot {L_0}^2 \cdot {\xi_0}^2 \tag{A6}$$

where $\rho = \frac{2 \cdot \overline{k_{IN}} \cdot L_0}{\overline{F_y}}$ is a non-dimensional parameter.

The level of approximation associated to the direct design equation can be assessed by comparing the values of the target mechanical parameters ($\overline{k_{IN}}$, $\overline{F_y}$ and $\overline{\mu}$) with the approximated corresponding ones of (k_{IN}, F_y and μ) calculated according to Eqs. A1, A2 and A3 using ξ_0, h and J as given by Eq. A4,A5,A6. In general, the approximated values of $k_{IN,CSB}$, $F_{y,CSB}$ and μ_{CSB} will differ from the corresponding target ones ($\overline{k_{IN,CSB}}$, $\overline{F_{y,CSB}}$ and $\overline{\mu_{CSB}}$), since the direct design equations have been derived based on the above-mentioned simplified assumptions.

Table A1 reports the relative errors between the target values $\overline{k_{IN,CSB}}$, $\overline{F_{y,CSB}}$, and $\overline{\mu_{CSB}}$, and the corresponding approximate values of $k_{IN,CSB}$, $F_{y,CSB}$ and μ_{CSB}. The relative error is computed as *e=(approximated value – target value) / target value* and is expressed in %. In almost all cases, the relative error is smaller than 10% for all the mechanical parameters.

Table A1: Target vs approximated values.

CSB number	Target mechanical parameters			Approximated mechanical parameters			Relative errors		
	$\overline{k_{in}}$ [kN/mm]	$\overline{F_y}$ [kN]	$\overline{\mu}$ [-]	k_{IN} [kN/mm]	F_y [kN]	μ [-]	e_K [%]	e_F [%]	e_μ [%]
CSB1	2.46	45.64	3.0	2.33	42.33	2.9	-5.2	-7.2	-3.1
CSB2	2.31	42.58	3.0	2.16	40.16	2.8	-6.6	-5.7	-5.5
CSB3	2.12	38.44	3.0	2.16	40.16	2.8	1.7	4.5	-5.5
CSB4	1.97	35.80	3.0	1.81	33.70	2.8	-8.1	-5.9	-5.5
CSB5	1.93	34.83	3.0	1.81	33.70	2.8	-6.2	-3.1	-5.5
CSB6	1.88	33.95	3.0	1.81	33.70	2.8	-3.7	-0.7	-5.5
CSB7	1.65	29.45	3.0	1.46	27.19	2.8	-11.5	-7.7	-5.5
CSB8	1.55	27.62	3.0	1.46	27.19	2.8	-5.8	-1.5	-5.5
CSB9	1.43	25.43	3.0	1.46	27.19	2.8	2.1	6.9	-5.5
CSB10	1.08	19.12	3.0	1.10	20.52	2.8	2.1	7.3	-5.5

References

[1] V. SEAOC, Committee (1995) performance-based seismic engineering for buildings, 2000.

[2] Y. Bozorgnia, V.V. Bertero, Earthquake engineering: from engineering seismology to performance-based engineering, CRC press, 2004. https://doi.org/10.1017/CBO9781107415324.004.

[3] J.M. Kelly, Base isolation: linear theory and design, Earthq. Spectra. 6 (1990) 223–244.

[4] C. Christopoulos, A. Filiatrault, V.V. Bertero, Principles of passive supplemental damping and seismic isolation, IUSS Press. (2006).

[5] M. Baiguera, G. Vasdravellis, T.L. Karavasilis, Dual seismic-resistant steel frame with high post-yield stiffness energy-dissipative braces for residual drift reduction, J. Constr. Steel Res. 122 (2016) 198–212.

[6] J.J. Ajrab, G. Pekcan, J.B. Mander, Rocking wall--frame structures with supplemental tendon systems, J. Struct. Eng. 130 (2004) 895–903.

[7] M.A. Jiun-Wei Lai1 and Stephen A. Mahin, Strongback System: A Way to Reduce Damage Concentration in Steel-Braced Frames, ASCE J. Struct. Eng. 1 (2007) 1–18. https://doi.org/10.1061/(ASCE)ST.1943-541X.

[8] M. Palermo, V. Laghi, G. Gasparini, T. Trombetti, Coupled Response of Frame Structures Connected to a Strongback, J. Struct. Eng. (United States). 144 (2018) 1–19. https://doi.org/10.1061/(ASCE)ST.1943-541X.0002134.

[9] M. Palermo, V. Laghi, G. Gasparini, S. Silvestri, T. Trombetti, Seismic Design and Performances of Frame Structures Connected to a Strongback System and Equipped with Different Configurations of Supplemental Viscous Dampers, Front. Built Environ. 7 (2021) 748087.

[10] M. D'Aniello, G. La Manna Ambrosino, F. Portioli, R. Landolfo, Modelling aspects of the seismic response of steel concentric braced frames, Steel Compos. Struct. 15 (2013) 539–566. https://doi.org/10.12989/scs.2013.15.5.539.

[11] P. Castaldo, M. De Iuliis, Optimal integrated seismic design of structural and viscoelastic bracing-damper systems, Earthq. Eng. \& Struct. Dyn. 43 (2014) 1809–1827.

[12] R. Tremblay, Inelastic seismic response of steel bracing members, J. Constr. Steel Res. (2002). https://doi.org/10.1016/S0143-974X(01)00104-3.

[13] G. Della Corte, M. D'Aniello, R. Landolfo, F.M. Mazzolani, Review of steel buckling-restrained braces, Steel Constr. 4 (2011) 85–93.

[14] P. Castaldo, E. Tubaldi, F. Selvi, L. Gioiella, Seismic performance of an existing RC structure retrofitted with buckling restrained braces, J. Build. Eng. 33 (2021) 101688.

[15] E. Nobahar, B. Asgarian, O. Mercan, S. Soroushian, A post-tensioned self-centering yielding brace system: development and performance-based seismic analysis, Struct. Infrastruct. Eng. (2020) 1–21.

[16] S. Maleki, S. Bagheri, Pipe damper, Part I: Experimental and analytical study, J. Constr. Steel Res. (2010). https://doi.org/10.1016/j.jcsr.2010.03.010.

[17] H.N. Li, G. Li, Experimental study of structure with "dual function" metallic dampers, Eng. Struct. (2007). https://doi.org/10.1016/j.engstruct.2006.10.007.

[18] S. Kato, Y.B. Kim, S. Nakazawa, T. Ohya, Simulation of the cyclic behavior of J-shaped steel hysteresis devices and study on the efficiency for reducing earthquake responses of space structures, J. Constr. Steel Res. (2005). https://doi.org/10.1016/j.jcsr.2005.03.006.

[19] N.N. Pujari, Optimum Placement of X-Plate Dampers for Seismic Response Control of Multistoried Buildings, October. 04 (2011) 481–485.

[20] M. Nakashima, S. Iwai, M. Iwata, T. Takeuchi, S. Konomi, T. Akazawa, K. Saburi, Energy dissipation behaviour of shear panels made of low yield steel, Earthq. Eng. Struct. Dyn. 23 (1994) 1299–1313.

[21] R.W.K. Chan, F. Albermani, Experimental study of steel slit damper for passive energy dissipation, Eng. Struct. (2008). https://doi.org/10.1016/j.engstruct.2007.07.005.

[22] H.-L. Hsu, H. Halim, Improving seismic performance of framed structures with steel curved dampers, Eng. Struct. 130 (2017) 99–111.

[23] H.-L. Hsu, H. Halim, Brace performance with steel curved dampers and amplified deformation mechanisms, Eng. Struct. 175 (2018) 628–644.

[24] L.-J. Jia, H. Ge, R. Maruyama, K. Shinohara, Development of a novel high-performance all-steel fish-bone shaped buckling-restrained brace, Eng. Struct. 138 (2017) 105–119.

[25] M. Khalili, A. Sivandi-Pour, E.N. Farsangi, Experimental and numerical investigations of a new hysteretic damper for seismic resilient steel moment connections, J. Build. Eng. 43 (2021) 102811.

[26] W. Guo, S. Li, Z. Zhai, Z. Li, S. Tan, F. Ding, Seismic performance of a new S-shaped mild steel damper with varied yielding cross-sections, J. Build. Eng. 45 (2022) 103508.

[27] G. Xu, J. Ou, Seismic performance of combined rotational friction and flexural yielding metallic dampers, J. Build. Eng. 49 (2022) 104059.

[28] S.A. Freeman, The capacity spectrum method, in: 11th Eur. Conf. Earthq. Eng., Paris, 1998.

[29] T. Trombetti, S. Silvestri, G. Gasparini, I. Ricci, Stiffness-Strength-Ductility-Design Approaches for Crescent Shaped Braces, Open Constr. Build. Technol. J. 3 (2009) 127–140. https://doi.org/10.2174/1874836800903020127.

[30] M. Palermo, I. Ricci, S. Gagliardi, S. Silvestri, T. Trombetti, G. Gasparini, Multi-performance seismic design through an enhanced first-storey isolation system, Eng. Struct. (2014). https://doi.org/10.1016/j.engstruct.2013.11.002.

[31] M. Palermo, S. Silvestri, G. Gasparini, T. Trombetti, Crescent shaped braces for the seismic design of building structures, Mater. Struct. 48 (2015) 1485–1502. https://doi.org/10.1617/s11527-014-0249-z.

[32] O. Kammouh, S. Silvestri, M. Palermo, G.P. Cimellaro, Performance-based seismic design of multistory frame structures equipped with crescent-shaped brace, Struct. Control Heal. Monit. 25 (2018) 1–17. https://doi.org/10.1002/stc.2079.

[33] M. Palermo, L. Pieraccini, A. Dib, S. Silvestri, T. Trombetti, Experimental tests on Crescent Shaped Braces hysteretic devices, Eng. Struct. 144 (2017) 185–200. https://doi.org/10.1016/j.engstruct.2017.04.034.

[34] M. Fintel, F.R. Khan, Shock-Absorbing Soft Story Concept for Multistory Earthquake Structures, ACI J. Proc. 66 (n.d.). https://doi.org/10.14359/7365.

[35] M. Palermo, V. Laghi, G. Gasparini, S. Silvestri, T. Trombetti, Analytical estimation of the key performance points of the tensile force-displacement response of Crescent Shaped Braces, Soil Dyn. Earthq. Eng. 148 (2021) 106839.

[36] E. Mokhtari, V. Laghi, M. Palermo, S. Silvestri, Quasi-static cyclic tests on a half-scaled two-storey steel frame equipped with Crescent Shaped Braces, Eng. Struct. 232 (2021). https://doi.org/10.1016/j.engstruct.2020.111836.

[37] E. Mokhtari, M. Palermo, V. Laghi, A. Incerti, C. Mazzotti, S. Silvestri, Quasi-static cyclic tests on a half-scaled two-storey steel frame equipped with Crescent Shaped Braces at both storeys: Experimental vs. numerical response, J. Build. Eng. (2022). https://doi.org/https://doi.org/10.1016/j.jobe.2022.105371.

[38] R.D. Bertero, V. V. Bertero, Performance-based seismic engineering: The need for a reliable conceptual comprehensive approach, Earthq. Eng. Struct. Dyn. 31 (2002) 627–652. https://doi.org/10.1002/eqe.146.

[39] M. Palermo, I. Ricci, S. Gagliardi, S. Silvestri, T. Trombetti, G. Gasparini, Multi-performance seismic design through an enhanced first-storey isolation system, Eng. Struct. 59 (2014) 495–506.

[40] O. Lavan, R. Levy, Optimal peripheral drift control of 3D irregular framed structures using supplemental viscous dampers, J. Earthq. Eng. 10 (2006) 903–923.

[41] A.K. Chopra, Dynamics of structures, (1975).

[42] G. Ballio, F.M. Mazzolani, Strutture in acciaio, Arnoldo Mondadori Editore, 1979.

[43] P. Pozzati, C. Ceccoli, Teoria e tecnica delle strutture, Utet, 1972.

[44] SAP2000, (n.d.). www.csiamerica.com/products/sap2000.

[45] D. Gasparini, E.H. Vanmarcke, SIMQKE: A program for artificial motion generation, Dep. Civ. Eng. Massachusetts Inst. Technol. Cambridge, MA. 2139 (1976).

[46] M. delle I. e Trasporti, Aggiornamento delle Norme Tecniche per le Costruzioni, 2018.

[47] J.W. Baker, Conditional mean spectrum: Tool for ground-motion selection, J. Struct. Eng. 137 (2011) 322–331.

[48] P. Castaldo, G. Amendola, Optimal sliding friction coefficients for isolated viaducts and bridges: A comparison study, Struct. Control Heal. Monit. 28 (2021) e2838.

[49] S. Kitayama, M.C. Constantinou, Collapse performance of seismically isolated buildings designed by the procedures of ASCE/SEI 7, Eng. Struct. 164 (2018) 243–258.

[50] S. Kitayama, M.C. Constantinou, Probabilistic seismic performance assessment of seismically isolated buildings designed by the procedures of ASCE/SEI 7 and other enhanced criteria, Eng. Struct. 179 (2019) 566–582.

[51] M. Palermo, S. Silvestri, G. Gasparini, T. Trombetti, A statistical study on the peak ground parameters and amplification factors for an updated design displacement spectrum and a criterion for the selection of recorded ground motions, Eng. Struct. 76 (2014) 163–176.

[52] S.E.E. SoftwareSolutions, SeismoStruct, (n.d.). http://www.seismosoft.com/en/HomePage.aspx.

[53] E. Spacone, V. Ciampi, F.C. Filippou, Mixed formulation of nonlinear beam finite element, Comput. Struct. (1996). https://doi.org/10.1016/0045-7949(95)00103-N.

[54] A.A. Correia, F.B.E. Virtuoso, Nonlinear analysis of space frames, in: 3rd Eur. Conf. Comput. Mech. Solids, Struct. Coupled Probl. Eng., Lisbon, Portugal, 2006.

[55] F.C. Filippou, E.P. Popov, V.V. Bertero, Effects of Bond Deterioration on Hysteretic Behaviour of Reinforced Concrete Joints. Report to the National Science Foundation, Earthq. Eng. Res. Cent. (1983) 1–212. http://www.ce.berkeley.edu/~filippou/Research/Publications/Reports/EERC-83-19.pdf.

[56] P. Castaldo, D. Gino, G. Bertagnoli, G. Mancini, Resistance model uncertainty in non-linear finite element analyses of cyclically loaded reinforced concrete systems, Eng. Struct. 211 (2020) 110496.

[57] A.M. Mwafy, A.S. Elnashai, Static pushover versus dynamic collapse analysis of RC buildings, Eng. Struct. 23 (2001) 407–424.

[58] H. Heidkamp, I. Papaioannou, Performance Based Design and Eurocode, 3rd Int. Symp. Geotech. Saf. Risk,. (2011) 519–526. http://vzb.baw.de/e-medien/geotechnical-safety-and-risk-2011/PDF/4 Codes and Standards/4_08.pdf.